High Voltage Grounding Systems

by

Gary Gilbert

A thesis
presented to the University of Waterloo
in fulfillment of the
thesis requirement for the degree of
Doctor of Philosophy
in
Electrical and Computer Engineering

Waterloo, Ontario, Canada, 2011

Author's Declaration

I hereby declare that I am the sole author of this thesis. This is a true copy of the thesis, including any required final revisions, as accepted by my examiners.

I understand that my thesis may be made electronically available to the public.

Abstract

Minimization of Construction Costs of Substation Grounding Grids

In every electrical installation, one of the most important aspects is adequate grounding; in particular, the grounding of high-voltage substations to protect people and equipment in the event of an electrical fault. Well-designed grounding systems ensure the performance of power systems and safety of personnel. It is desirable that the substation grounding provides a near zero resistance to remote earth. The prevailing practice of most utilities is to install a grid of horizontal ground electrodes (buried bare copper conductors) supplemented by a number of vertical ground rods connected to the grid, and by a number of equipment grounding mats and interconnecting cables. The grounding grid provides a common ground for the electrical equipment and for all metallic structures at the station. It also limits the surface potential gradient. Currently the IEEE 80-2000 standard for substations grounding [1] limits the determination of the grounding parameters (namely step, touch and ground potential rise) to that of a uniform soil model unless the Sunde graphical method is used. With the Sunde graphical method, it relies on interpretation to obtain a two layer soil model. Without the use of the graphical method, the IEEE 81-1983 [2] has several empirical equations that can be used for the two layer model; however, these equations rely on the use of images which retard the speed of calculations to the point where the overall optimization of the grounding grid (with respect to size and shape) has yet to be determined.

The goal of the thesis was to improve upon the current restrictions for the grounding grid design, while minimizing the material (i.e., copper conductors) and installation costs of a grid. The first part of the research examined previous work through a combination of literature review, mathematical computations, and field measurements to validate the theoretical aspects of grid design. The thesis introduces an optimized uniform and two-layer soil with fast accurate calculations directly from soil measurements without the use of graphical methods or the use of complex image theory. Next, the thesis develops enhanced grounding parameter equations using Simpson's Rule of integration. The final part of the thesis demonstrates how it is possible to optimize the configuration of the grounding grid itself, minimizing costs, and yet still achieving a safe installation. This is the first time such an optimization is possible, and it is made possible by the techniques developed in this thesis. The techniques are applied to existing real-world grid

designs, and the results obtained show the effectiveness of the method in reducing construction costs. This thesis shows how these construction and material savings are realized by utilizing a process whereby the grounding design minimizes the overall cost. The overall contribution of this thesis is the optimization of the grounding grid design by eliminating the current restrictions found in the IEEE standards 80 and 81, respectively, and offering an optimized grounding system design, starting from the soil model to the actual grounding design itself.

Acknowledgements

I wish to express my gratitude to Professor Chow, Professor Salama and Dr Bouchard for their time, patience and direction in helping me succeed at this work. For this, I will always be indebted.

Dedication

To my wife, Catherine, and our two, children, Siobhan and Gary

Table of Contents

List of Figures

List of Tables

Chapter 1 Introduction

1.0 Preface

In every electrical installation, one of the most important aspects is adequate grounding; more specifically, the grounding of high-voltage substations to protect people and equipment in the event of an electrical fault. Well-designed grounding systems ensure the performance of power systems and safety of personnel. Design procedures, however, are often hindered by a number of factors that are difficult to quantify. Based primarily on experience and simple analytical models, the first guide for the design of substation grounding systems was introduced in 1961: the ANSI/IEEE Std 80-2000 [1]. This document, together with three major revisions in 1976, 1986, and 2000, has been the primary tool available to substation engineers for analysis and design of substation grounding systems. The IEEE Std 80-2000 is limited to the uniform soil model, which is not found in many substation locations; however the IEEE Std 81-1983 [2] offers empirical solutions for the two layer soil model. The empirical solutions offered within this standard still rely on complex image theory which drastically slows the computational speed of the solution whereby researchers are limited with its usage.

When there is a ground fault at a substation, the flow of ground current depends on the impedances of the various possible paths. Currents may flow between portions of the substation ground grid, between the ground grid and the surrounding earth (i.e. out of the substation area), along overhead sky wires, or along a combination of all these paths. The potential rise of a substation when a current is flowing through its ground must be limited to a safe value so that there is no danger to anyone touching conductive material, such as the substation fence. Figure 1.1 demonstrates the step, touch and the ground potential rise voltages that a worker could be subjected in the event of a ground fault.

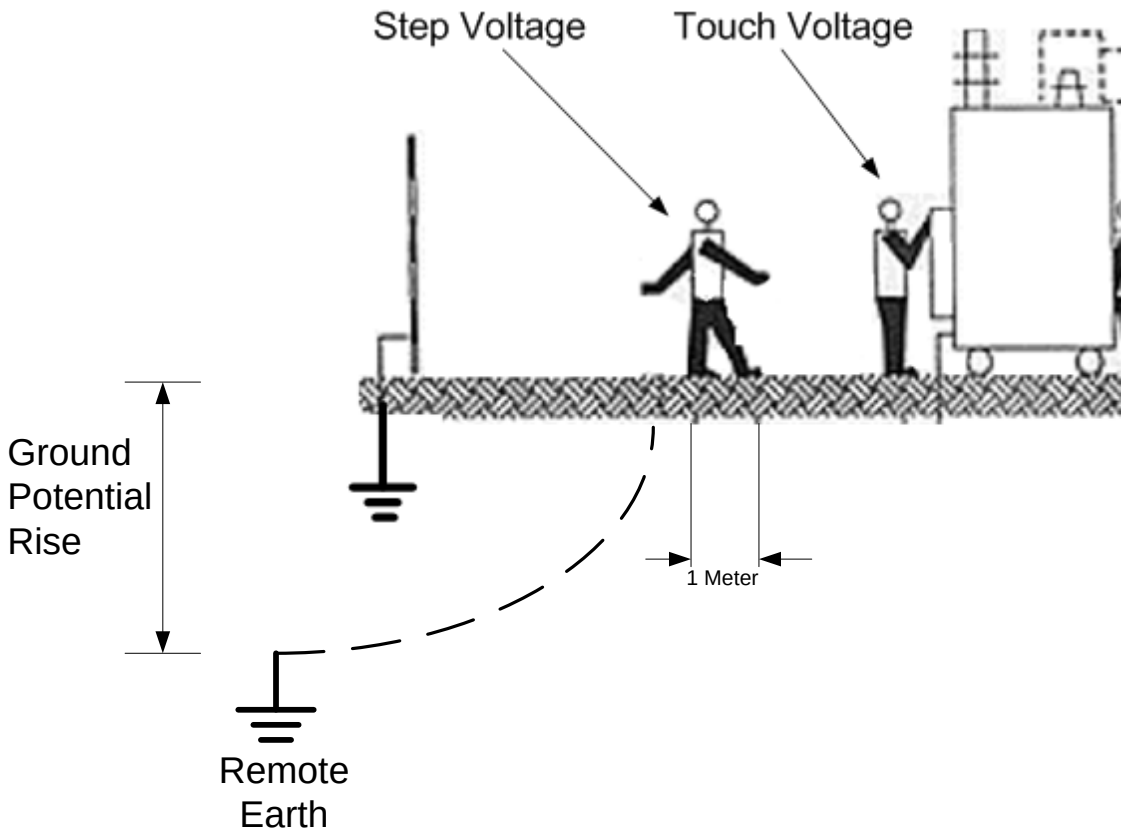

Figure 1.1 Step and touch voltages, and ground potential rise (GPR)

The ground potential rise (GPR) at the station is equal to the current flowing between the ground and the surrounding earth multiplied by the station grounding resistance in relation to remote earth. It is desirable that the substation grounding system provide a low impedance path to allow for the fast safe dissipation of any and all fault currents. The prevailing practice of most utilities is to install a grid of horizontal ground electrodes (buried bare copper conductors) supplemented by a number of vertical ground rods connected to the grid, and by a number of equipment grounding mats and interconnecting cables. The grounding grid provides a common ground for the electrical equipment and for all metallic structures at the station. It also limits the surface potential gradient. The vertical ground rods decrease the overall resistance of the substation. There are three variables that affect the resistance of the ground rods.

1.) The ground itself can affect the resistance of the ground rods. The soil around the rods is seldom homogeneous and resistance values can vary greatly.

2.) The depth of the ground electrode can affect the resistance of the ground rods. This is a very effective way of decreasing substation resistance. The earth is in layers and the

resistivity of each layer considerably changes from layer to layer. Generally, doubling the length of the rod can decrease resistance by about 40%. Most of the rod is below frost level so freezing will not considerably increase the substation resistance.

3.) The diameter of the ground electrode can affect the resistance of the ground rods. The diameter of the rod affects the resistance but the effect is not very large. Doubling the diameter of the rod will decrease the rod resistance by only 10 %.

Each grounding rod has its sphere of influence and, to be effective, the rods cannot be crowded. In general, the spacing between the rods should not be less than the depth to which they are driven.

The flow of ground current between parts of the ground gives rise to a step potential. Step potential is defined as the difference in surface potential experienced by a person bridging a distance of 1 m with his feet without contacting any other grounded object. The value of the maximum safe step potential depends on the resistivity of the top layer of surface material, and on the duration of the current flow. For example, for a substation with a 10 cm layer of crushed rock and current flowing for 0.5 s, the maximum allowable step potential is approximately 3100V in accordance with [1]. Touch potential is the potential difference between a surface potential at a point where a person is standing, and a grounded metallic structure at a normal maximum reach (1 m). For the same situation as above, the maximum safe touch potential is approximately 880 V. A grounding network dissipates electrical fault currents into the earth without producing harmful voltage gradients that could be lethal to humans. To ensure fault currents are dissipated in a safe manner, three parameters must be calculated: ground potential rise (GPR), step voltages as defined in [1], and touch voltages as defined in [1]. As discussed in [2], if the measured ground resistance is found to be consistent with the calculated ground grid resistance, there is reasonable assurance that the step and touch voltages will not be suspect. These step and touch voltage limits are selected such that the possible electric body current in an operator or bystander should not exceed the defined limit under any adverse conditions [1, 2].

In the case where a simple soil model is used to calculate the grounding resistance of the grid, the deviation between the measured values and calculated values will be large if the soil is not uniform in nature. In this case, the designer has two options, which can create a difficult choice. The first option is to redesign the grounding grid in order to meet the step and touch voltage limit and then rebuild the grounding system. The second option is to try to add more

rods to the grid, in a trial-and-error fashion, measuring the grounding resistance after each addition. Both options are costly in terms of material and manpower, and, in cases of complicated substation grounding systems; safe limits cannot always be achieved.

The goal of this thesis is to improve upon ground grid design, minimizing the total cost of the material and installation costs of the grounding grid. To this end, this thesis offers a novel technique which optimizes the design. A new optimization will reduce the material and installation costs in multilayer soil by utilizing a simple, fast and time tested two-layer soil model. The first part of the research will examine previous work and outline the grounding grids with various types of soil models [3-12]. This section is a combination of literature review, mathematical computations, and field measurements to validate the theoretical aspects of the design. It has already been shown that the two-layer soil model yields more accurate results than the single-layered soil model when the soil is not uniform in nature [3]. This makes it desirable to ensure an accurate soil model is achieved.

With the improved efficiency and speed of the determination of the grounding grid parameters, it is then possible to investigate the optimization of the grounding grid. The grounding grid will have optimized parameters, which include the grid spacing, number of ground rods, and conductor length of a predefined ground grid topology. The focus of optimization of the grounding grid will be directed to larger grounding grids in which the costs of material and installation are significant. This work has never been attempted due to the complexity of the problem when using the current complex images needed with more than one soil layer. By eliminating the requirement for the use of complex images, the computational burden is reduced. The grounding resistance can then be calculated directly, rapidly decreasing the computational time with the use of the Galerkin Moment Method.

1.1 Thesis Objectives and Scope of Work

The main objective of the thesis was the development of new efficient techniques to determine the grounding grid design. This objective can be broken down into the following:

Soil Model Objective

- Develop a soil model directly with fast accurate calculations directly from field measurements, eliminating the Sunde graphical method [1, 9] and the current empirical equations that use images.

Grounding Parameter Equations Objective

- Develop new strategies for computing grounding resistance, step and touch voltages by the use of Simpson's rule of integration to speed up the calculation process for the grounding grid itself.

Grounding Grid Optimization Objectives

- Develop a method to minimize construction and material costs of a grounding grid while still satisfying maximum GPR, and step and touch voltages.

1.2 Thesis Layout

Chapter 1 provides an introduction in regards to grounding system design. It then outlines the thesis objectives and scope of work.

Chapter 2, *Soil Structure, Test Procedure, Soil Modeling,* begins with a literature survey of existing soil structures and test procedures currently used in industry. Soil model determination used in grounding grid design has been developed significantly since the approximation produced by the graphical Sunde method [9], which provided a good approximation for the uniform and two-layer soil model, but was prone to errors. A new approach in the determination of the soil structure is proposed that optimally determines the soil model used in the grounding system design.

Chapter 3, A *Simple Formula for Sunde's Curves and its Use in Automatic Extraction of Soil Layers from Field Measurements,* offers a numerical closed form solution to find the soil parameters of a two-layer soil model. This solution proposes the use of field measurements to generate an optimized two-layer model.

Chapter 4, *Grounding System Design Equations,* begins with a literature survey of the current methods of numerically determining the safety criteria in the various soil models discussed earlier. This chapter focuses on these existing methods like the finite element method and the traditional equations used in the standards and how researchers are at an impasse in improving the speed and accuracy of the computations. The chapter then shows how this impasse is overcome and improved, by using the Galerkin Moment Method in the optimization of the grounding design in Chapter 5.

Chapter 5, *Optimization of the Grounding Grid*, begins with a literature survey of the current means of achieving the optimization of the grounding grid to reduce the material and installation costs. The chapter illustrates how the optimization will reduce costs without jeopardizing safety.

Chapter 6, *Conclusions and Recommendations***,** is a review of the three aspects of the research presented within the thesis and provides conclusions and recommendations for future work, including the soil model development, the grounding parameter equation enhancements and the overall optimization of the grounding grid itself.

Chapter 2 Soil Structure, Test Procedure and Soil Modeling

2.0 Introduction

The main objective of grounding electrical systems is to provide a suitably low resistance connection to the substation. The low resistance is to limit the potential rise of the substation from the potential of the surrounding earth [1]. This potential rise must be limited so that there is no danger to anyone standing on the ground but touching, for example, the substation fence. In order to ensure that the ground potential rise, and touch and step voltages are within safe limits, an accurate soil model is needed to ensure that the resistance of the grounding grid is sufficiently low. This soil model comes from the field measurements of the soil structure at the proposed grid location. This chapter provides a literature survey of the various soil testing methods and soil modeling. The chapter is divided into 2 parts: Part 1 describes the current soil measurement techniques; Part 2 examines the model construction of the uniform and two-layer soil structures, and the shortcomings of the current modeling techniques.

2.1 Soil Resistivity and Structure

Resistance is the property of a conductor that opposes electric current flow when a voltage is applied across the two ends of a linear conductor. The unit of measure for resistance is the Ohm (Ω), and the commonly used symbol is *R*. The resistance of a conductor depends on the atomic structure of the material or its resistivity (measured in Ω.m), and it can be calculated from the resistivity of the conductor using the standard definition of (2.1):

$$R = \frac{\rho * L}{A} \tag{2.1}$$

where: ρ is the resistivity (Ω.m) of the conductor material

L is the length of the conductor (m)

A is the cross sectional Area (m^2)

Equivalent to (2.1), soil resistivity can be defined as the resistance between the opposite sides of a cube of soil with a side dimension of one meter. Soil resistivity values vary widely, depending on the type of terrain; e.g., silt on a riverbank may have a resistivity value around 1.5 Ω.m, whereas dry sand or granite in mountainous country may have values higher than 10,000 Ω.m. The factors that affect resistivity may be summarized as follows [2]:

- Type of earth (e.g., clay, loam, sandstone, granite).

- Stratification of layers of different types of soil (e.g., loam backfill on a clay base).
- Moisture content: resistivity may fall rapidly as the moisture content is increased, but after a value of about 20%, the rate of change in resistivity is much less. Soil with moisture content greater than 40% is rarely encountered.
- Temperature: above and below the freezing point, the effect of temperature on earth resistivity changes the resistivity significantly. The seasonal changes are not currently enforced in several parts of the world; however, they should be considered [1].
- Chemical composition and concentration of dissolved salts. Presence of metal and concrete pipes, tanks, large slabs, cable ducts, rail tracks, or metal pipes. Figure 2.1 shows how resistivity varies with salt content, moisture, and temperature.

It is found that earth resistivity varies from 0.01 to 1 Ω.m for sea water, and up to 10^9Ω.m for sandstone [2]. The resistivity of the earth increases slowly with decreasing temperatures from 25^{o}C, while for temperatures below 0^{o}C, the resistivity increases rapidly. In frozen soil, as in the surface layer in winter, the resistivity may be exceptionally high. Table 2.1 shows the resistivity values for various soils and rocks that might occur in different grounding system designs.

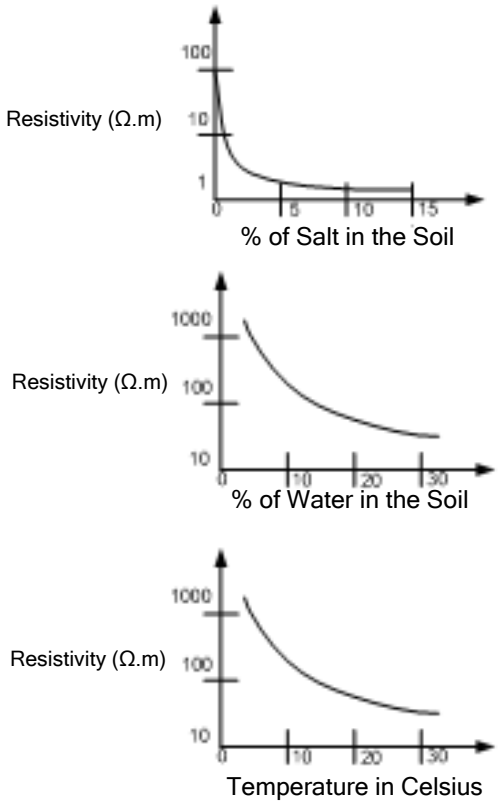

Figure 2.1 Soil resistivity variations [2].

Table 2.1 Resistivity values for several types of soils and water 25°C [2].

Type of Soil or Water	**Typical Resistivity (Ω.m)**	**Usual Limit (Ω.m)**
Sea water	2	0.1 to 10
Clay	40	8 to 70
Ground well and spring water	50	10 to 150
Clay and sand mixtures	100	4 to 300
Shale, slates, sandstone, etc.	120	10 to 100
Peat, loam, and mud	150	5 to 250
Lake and brook water	250	100 to 400
Sand	2000	200 to 3000
Moraine gravel	3000	40 to 10000
Ridge gravel	15000	3000 to 30000
Granite	25000	10000 to 50000
Ice	100000	10000 to 100000

When defining the electrical properties of the earth, the geoelectric parameters are used in the determination of the soil model. These electrical properties of the soil are determined by the thickness of layers and their changes in resistivity. Usually there are several soil layers, each having a different resistivity, in which case the soil is said to be non-uniform. Lateral changes may also occur, but, in general, these changes are gradual and negligible, at least in the vicinity of a site where a grid is to be installed. In most cases, measurements will show that the resistivity, ρ, is mainly a function of depth. The interpretation of the measurements consists of establishing a simple equivalent function to yield the best approximation of soil resistivities to determine the layer model.

In the case of station grounding systems, a two-layer soil model (Figure 2.2) has been found to be a good approximation of the soil structure for ground system designs [3-10].

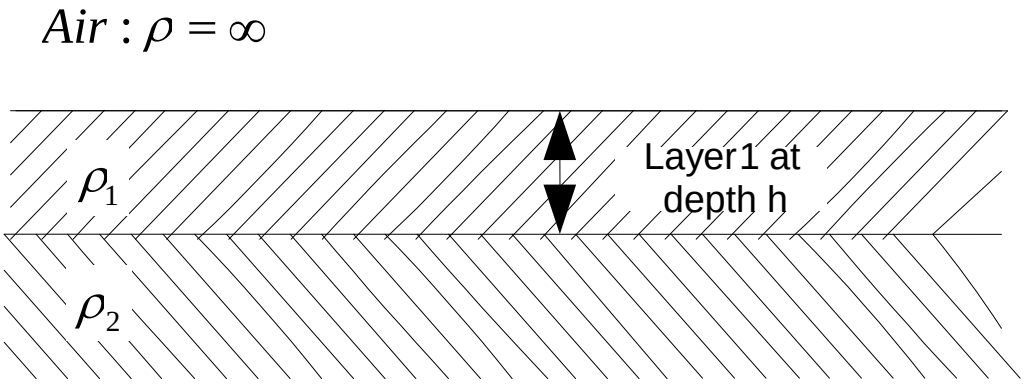

Figure 2.2 Two-layer soil model.

2.2 Review of Existing Soil Resistivity Measurement Procedures

Soil resistivity measurements are used to obtain a set of measurements that may be used to yield an equivalent soil model for the electrical performance of the earth. The results, however, may be unrealistic if adequate background investigation is not made prior to the measurement. The background investigation includes data related to the presence of nearby metallic structures, as well as the geological, geographical, and meteorological information of the area. For instance, geological data regarding strata types (soil layer) and thicknesses would give an indication of the water retention properties of the upper layers and therefore their expected variation in resistivity between the layers; then make a comparison of recent rainfall data against the seasonal average. Such background investigation is usually included as a part of the soil measurement procedure

and is used in the determination of the soil model to be used in the determination of the grounding grid resistance [2].

Soil resistivity measurements are made by injecting a current into the earth between two outer current probes and measuring the resulting voltage between two inner potential probes placed along the same straight line. When the adjacent current and potential probes are close together, the measured soil resistivity is indicative of the surface soil characteristics; however, more measurements would be required. When the probes are far apart, the measured soil resistivity is indicative of average deep soil characteristics throughout a much larger area. In principle, soil resistivity measurements are made using spacing (between adjacent current and potential probes) that are, at least, on the same order of magnitude as the maximum size of the grounding system (or systems) under study. It is, however, preferable to extend the measurement traverses to several times the maximum grounding system dimension, where possible. This allows for fine tuning of the soil model if there is more than one soil layer present. Often, it will be found that the maximum probe spacing is governed by other considerations, such as the maximum area of the available land which is clear of interfering bare buried conductors.

2.2.1 Soil Resistivity Measurements

Factors such as maximum probe depth, lengths of cables required, efficiency of the measuring technique, cost (determined by time and the size of the survey crew), and ease of interpretation of the data must be considered when selecting the test type. Three common test types are the Wenner 4-Probe Method, Schlumberger Array, and the Driven Rod (3-Probe) Method. These methods will be discussed below. In homogenous isotropic earth, the resistivity will be constant; however, if the earth is non-homogenous and the electrode spacing is varied, a different value of resistivity will be found for each surface measurement. This measured value of soil resistivity is referred to as the apparent resistivity, ρ_a as measurement is used in the calculation of the soil model and is not the actual value of resistivity. This reinforces the requirement for an accurate soil model. For the three common test types, the measurement techniques and the test methods' equations will be presented.

2.2.1.1 Wenner Array

In the Wenner method (See Figure 2.3), all four probes are moved for each test, with the spacing between each adjacent pair remaining the same [2]. In the Wenner 4-probe method, it is possible to measure the average resistivity of the soil between the two center probes to a depth equal to the probe spacing between adjacent probes. If the probe spacing is increased, then the average soil resistivity is measured to a greater depth. If the average resistivity increases as the probe spacing increases, there is a region of soil having resistivity at the greater depth.

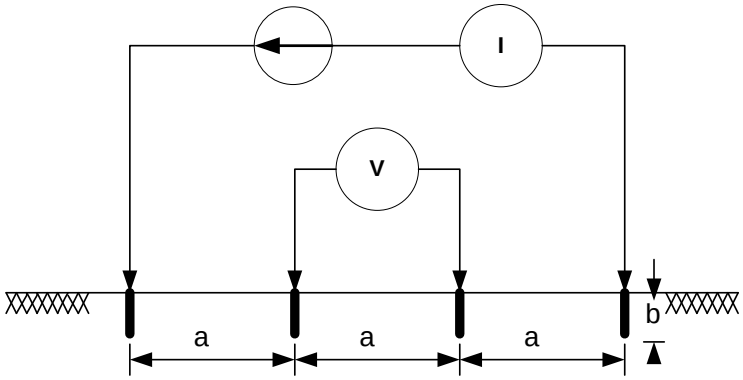

Figure 2.3 Wenner four-probe method.

Equation 2.2, determines the apparent resistivity based on the surface measurements as shown in Figure 2.3 if the penetration of the probe, *b*, is small compared to the spacing of the four probes (i.e., $a > 10b$) [2].

$$\rho_a = 2\pi aR \tag{2.2}$$

where: ρ_a is the apparent resistivity (Ω.m)

a is the probe spacing (m)

R is the measured resistance (Ω)

If the ratio between the penetrations of the probe *b* is similar to the spacing of the four probes, then (2.3) must be used as the apparent resistivity is matched closer to the probe depth. From [2], it is suggested that when there is more the one layer of soil this equation allows for greater accuracy in the determination of soil depths. This is a curve fitted equation, developed by Wenner.

$$\rho_a = \frac{4\pi aR}{1 + \frac{2a}{\sqrt{a^2 + 4b^2}} - \frac{a}{\sqrt{a^2 + b^2}}} \tag{2.3}$$

2.2.1.2 Schlumberger Array

The Schlumberger array (Figure 2.4) requires that the outer probes be moved four or five times for each position of the inner probes [2]. The reduction in the number of probe moves also reduces the effect of lateral variation in the test results. Considerable time savings can be achieved by using this method, since there will be fewer probe placements than those required by the Wenner method, with similar results. The minimum spacing accessible is in the order of 10m (for a 0.5 m inner spacing), thereby necessitating the use of the Wenner configuration for smaller spacing. Lower voltage readings are obtained when using the Schlumberger arrays. This may be a critical problem where the depth required to be tested is beyond the capability of the test equipment or the voltage readings are too small to be useful.

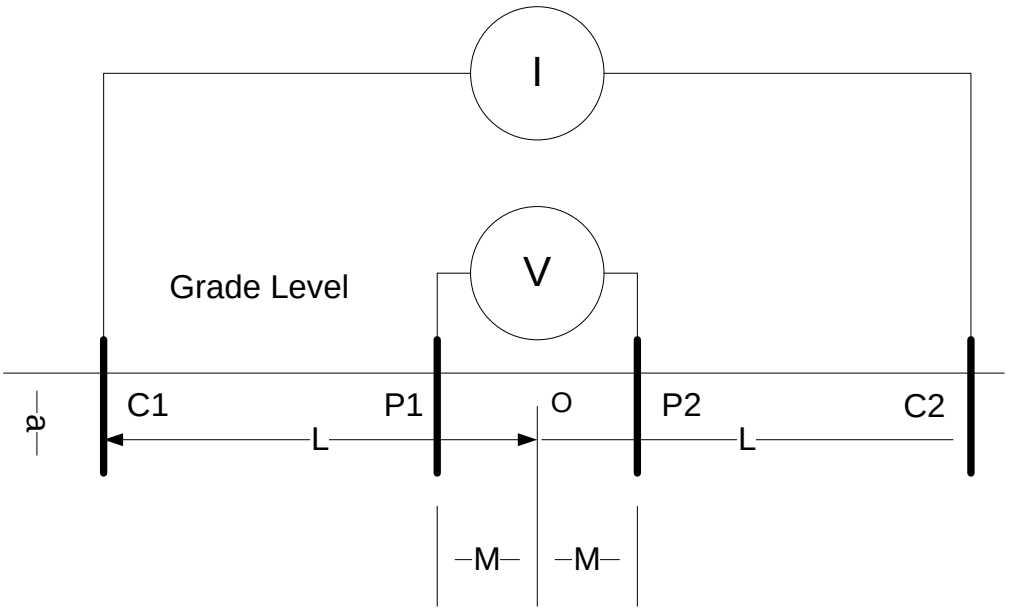

Figure 2.4 Schlumberger array.

The Schlumberger array is more complex, with the spacing between the current probes not equal to the spacing between the potential probes. Equation 2.4 determines the apparent resistivity based on the surface measurements as shown in Figure 2.4.

$$\rho_a = \frac{\pi L^2 R}{2M} \tag{2.4}$$

where: ρ_a is the apparent resistivity (Ω.m)

L is the distance from the center line to the outer probes (m)

M is the distance from the center line to the inner probes (m)

R is the measured resistance (Ω)

2.2.1.3 Driven Rod Method

The driven rod method (Figure 2.5) is generally employed where transmission line structures are located. This method is preferred because the measurements can be obtained without varying the spacing as required by the previous methods.

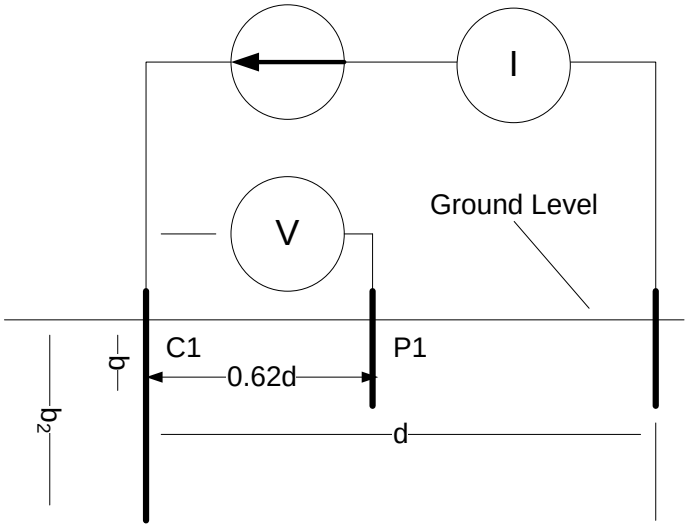

Figure 2.5 Driven Rod (3-Probe) method.

Equation 2.5 determines the apparent resistivity based on the surface measurements as shown in Figure 2.5.

$$\rho_a = \frac{2\pi b_2 R}{\ln\left(\frac{2b_2}{d}\right)} \tag{2.5}$$

where: ρ_a is the apparent resistivity (Ω.m)

b_2 is the length of the driven rod in contact with the earth (m)

d is the spacing between the current probes (m)

R is the measured resistance (Ω)

Significant tests from Ohio State University have demonstrated that all of the measurement techniques above yield similar results [11]. In the research, however, it was determined that there must be significant changes in the measurement spacings. For example, an increase of 1m to 2m in spacing would yield results significantly different than smaller incremental spacing changes, like from 1.1m to 1.2m.

2.2.2 Spacing Range

The range of spacings recommended in [11] includes accurate close probe spacings≤(m), which are required to determine the upper layer resistivity, used in calculating the step and touch voltages, to spacings larger than the radius or diagonal dimension of the proposed earth grid. The larger spacings are used in the calculation of remote voltage gradients and grid impedances. Measurements at very large spacings often present considerable problems. Such problems include inductive coupling, insufficient resolution of the test set, and physical barriers.

2.3 Determination of the Soil Structure

This part of the chapter introduces the uniform soil model and then a numerical solution for the two layer soil model, based on the soil parameters obtained through the testing methods discussed in section 2.2.1. In addition, this part of the chapter demonstrates the graphical method developed by Sunde [1].

2.3.1 Uniform Soil Model

Soil characteristics can be approximated from surface measurements, which provide a resistivity of the soil, ρ_a. If ρ_a is constant for various probe spacings, it is an indication that the earth at the measurement site is fairly uniform; otherwise, a two-layer model should be used. Figure 2.6 represents the soil structure for the uniform soil model.

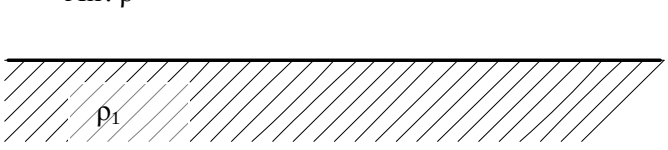

Figure 2.6 Uniform soil model.

The resistivity of a uniform soil model is determined by either (2.2) or (2.3), depending on whether the penetration of the probe, *b*, is small compared to the spacing of the four probes, and assumes the soil resistivity is uniform in nature to an infinite depth. After taking all of the surface measurements and determining the various resistivities at the substation location, an overall ρ_a for the grounding system can be determined. The IEEE 80-2000 standard [1] offers two equations for this calculation. The first equation is determined by an averaging of all of the measured values:

$$\rho_a = \frac{\rho_{a(1)} + \rho_{a(2)} + \rho_{a(3)} \cdots \rho_{a(n)}}{n} \tag{2.6}$$

where $\rho_{a(1)} + \rho_{a(2)} + \rho_{a(3)} \cdots \rho_{a(n)}$ are the measured apparent resistivity data obtained at different spacings by the methods discussed earlier, and *n* is the total number of measurements. The other equation that can be used is the following:

$$\rho_a = \frac{\rho_{a(\max)} + \rho_{a(\min)}}{2} \tag{2.7}$$

2.3.2 Two-Layer Soil Model

Typically, the observed resistivities vary when plotted as a function of the probe spacing. Large variations in probe spacing (a variance of greater than 30%) indicate that the earth is non-uniform, and a two-layer soil model must be used. Using a single-layer model in such a situation has been shown to cause significant errors in resistivities [3].

Figure 2.2 represents the two layered soil model, which has an upper layer of a finite depth, *h*, and resistivity, ρ_1, over a lower layer of infinite depth and resistivity, ρ_2. The difficulty in using this model is the mathematical determination of the depth of layer one, due to the numerous variations in the structure and properties of the earth. This research introduces a new technique that can be used for both the uniform and two layered models.

The methods used for interpolating the soil model from field measurements can be grouped into two categories: empirical or analytical. Empirical methods are typically developed through a combination of interpolation and field measurements. Sunde [1, 9] first proposed a graphical method to approximate a two-layer soil model, based on the interpretation of a series of curves which are commonly called the “Sunde curves,” and Figure 2.7 shows those curves.

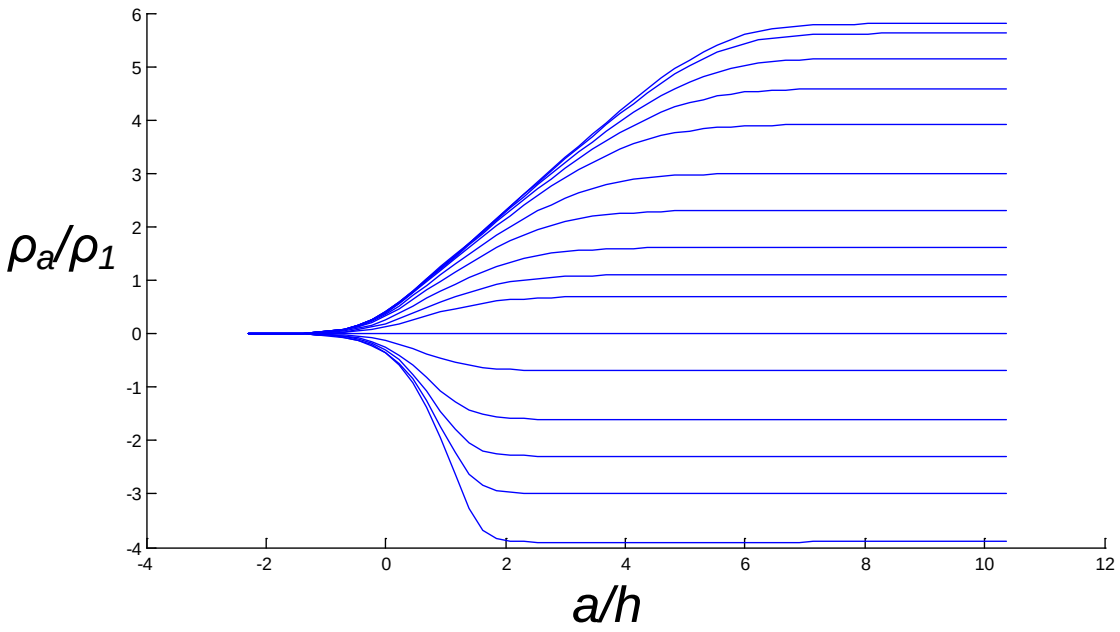

Figure 2.7 Sunde curves for two-layer soil structure from image theory.

Parameters ρ_1 and ρ_2 are obtained by inspection of resistivity measurements. The third parameter, *h*, is obtained by Sunde's graphical method, which is explained in detail in the IEEE Standard 80, along with an example [1]. In Sunde's method, the graph shown in Figure 2.7 is used to approximate a two-layer soil model, which is based on the Wenner four-pin test data or another method discussed earlier within the chapter. The parameters ρ_1 and ρ_2 are obtained by inspection of resistivity measurements and this is one of the limitations of the graphical methods as the designer begins the soil model determination by guessing. The parameter *h* is then obtained by Sunde's graphical method, as follows:

a) Plot a graph of apparent resistivity ρ_a on *y*-axis verses pin spacing on *x*-axis.

b) Estimate ρ_1 and ρ_2 from the graph plotted in (a). ρ_a corresponding to a smaller spacing is ρ_1 and for a larger spacing is ρ_2. Extend the apparent resistivity graph at both ends to obtain these extreme resistivity values if the field data are insufficient.

c) Determine ρ_2/ρ_1 and select a curve on the Sunde graph in Figure 2.7, which matches closely, or interpolate and draw a new curve on the graph.

d) Select the value on the *y*-axis of ρ_a/ρ_1 within the sloped region of the appropriate ρ_2/ρ_1 curve of from Figure 2.8.

e) Read the corresponding value of *a/h* on the *x*-axis.

f) Compute ρ_a by multiplying the selected value, ρ_a/ρ_1, in (d) by ρ_1.

g) Read the corresponding probe spacing from the apparent resistivity graph plotted in (a).

h) Compute *h*, the depth of the upper level, using the appropriate probe separation, *a*.

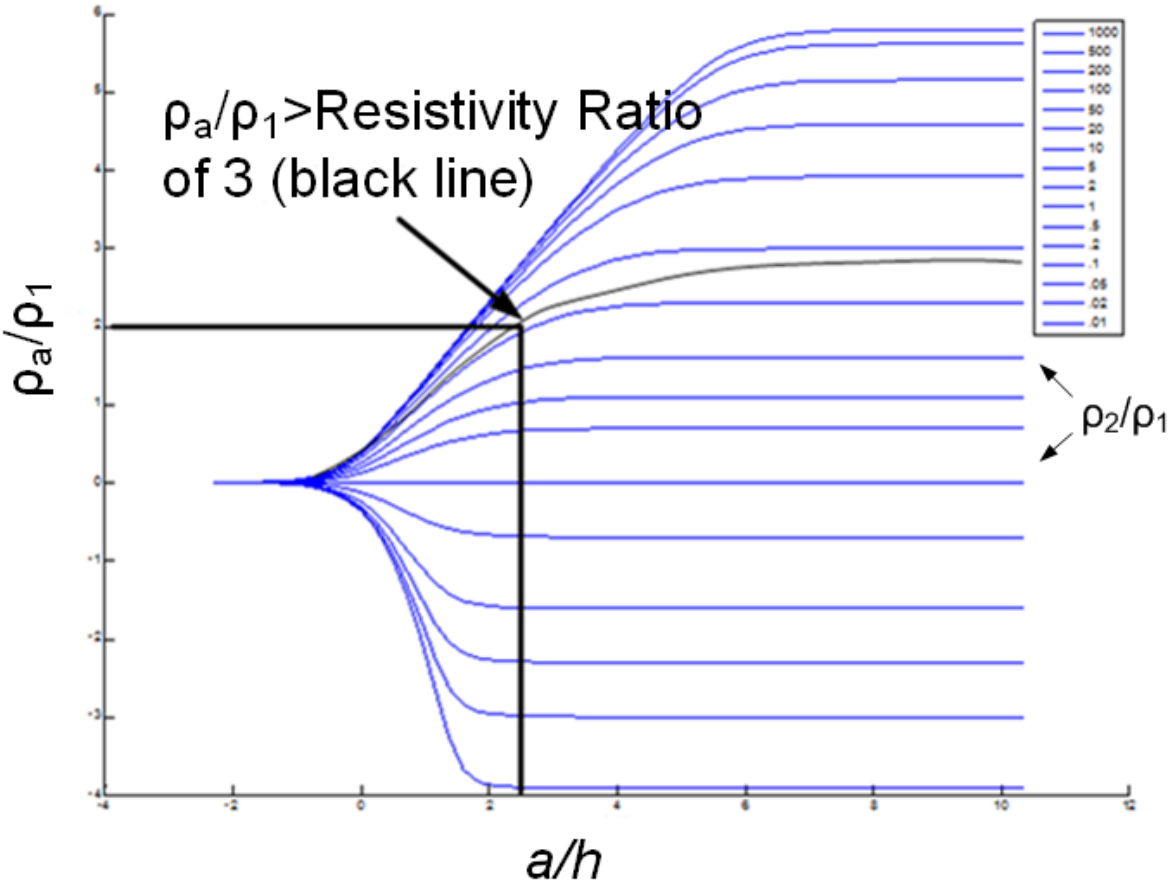

Figure 2.8 Sunde curves for two-layer soil structure from image theory.

The following example from [1] illustrates Sunde's graphical method from Figure 2.8, both ρ_1 and ρ_2 can be determined by visual inspection by first assuming that ρ_1 =100 Ω·m and ρ_2 = 300 Ω·m:

a) Plot Figure 2.8.

b) Choose ρ_1 =100 Ω·m, ρ_2 = 300 Ω·m

c) ρ_2/ρ_1 = 300/100 = 3 (resistivity ratio curve).

d) Select ρ_a/ρ_1 = 2.

e) Read a/h = 2.7 from Figure 2.8 for ρ_a/ρ_1 = 2.

f) Compute ρ_a: $\rho_a = 2\rho_1 = 2(100) = 200$.

h) Compute *h*: *h=a/(a/h)*, 19/2.7= 7.0m or 23 ft.

As one can see, the Sunde Curve allows for a rough approximation of the soil model parameters without the use of a computer or sophisticated equations and provides designers with a fundamental process to determine the soil model for many years. Due to the inaccuracies of the Sunde curves, as this method relies on the visual interpolation of the Sunde curves to determine the three soil model parameters, researchers were led to further Sunde's work. To this end, in [13], Dawalibi and Blattner found that the empirical solution obtained using the Sunde curves provided a rough approximation of the resistivities and the depth of the first layer in the two-layer model; however, they worked towards a more rigorous solution. The researchers developed a duplicate of the Sunde curves and provided a benchmark for a logarithmic curve-matching approach to determine the soil parameters [14 - 16]. The shortcoming of this method was that it was not an analytical solution, and relied on the Sunde curves themselves.

Seedher and Arora [17] introduced smoothening constants to enhance the equations of [1], which reduced the errors of both Sunde's and Dawalibi methods. The smoothening function proposed in [17] allowed for small fluctuations in the uniform soil approximation introduced by Sunde, but the fundamental equations for modeling remained the same, as this method also relied on the original Sunde's curves. In [18], Del Alamo compared several techniques used to estimate the soil parameters and improved on the evaluation of the parameters by introducing a Newton optimization process. Although there were reductions in the errors between the actual soil structure and the numerical one due to the optimization process, the technique was limited by the use of equations that were formulated by the Sunde's curves and the starting conditions of the optimization process itself. While the errors in the soil model parameter were reduced, the fundamental basis of the use of images remained the same in that the Sunde curves were used. More recently, Gonos and Stathopulos [19] successfully used a genetic algorithm to reduce errors in the soil model for the two-layer soil model. The technique developed by Gonos and Stathopoulos improved only the optimization process itself, and did not eliminate the use of complex images to determine the soil model parameters.

All of the algorithms mentioned above effectively match Sunde's curves, which are generated from complex images (in the actual physical space or its equivalent spectral space). The formula of the multiple complex images is an infinite series which is complicated and its behaviour is not easy to understand. Easy understanding would enhance the confidence of the

constructed soil model, and lead to better grounding grid designs, and possible design extension to three layer soils. By changing the existing method of Sunde's graphical method, researchers have found that an optimization process is required to improve the error of the constructed soil model. It would be helpful; therefore, if a simple analytical formula for the determination of the soil model parameters without the use of images could be found. Chapter 3 will derive such a formula, and demonstrate its effectiveness in the determination of the soil model itself.

2.4 Summary

This chapter provided a discussion of the parameters that affect grounding grid design, the importance of a good soil model, and a survey of existing techniques used to finds those models. One of the commonly used methods is the graphical Sunde method which is based on complex images. Researchers have advanced some of the original technique developed by the Sunde curves for comparison during calculations; however, there has been little effort in determining the soil model directly from the field measurements themselves.

Chapter 3 Novel and Simple Formula for Sunde's Curves and its Use in Automatic Extraction of Soil Layers from Field Measurements

3.0 Introduction

After reviewing the existing algorithms used to determine the soil model, it became apparent that it would be helpful if a simple analytical formula of the Sunde's curves could be found. This chapter will derive such a formula. The design of a grounding grid requires the development of a suitable mathematical model to represent the electrical properties of the earth in which the grid will be installed. Obtaining an accurate soil model can be difficult, as the soil typically has non-uniform characteristics. Often, the earth can be reasonably approximated by a two-layered soil structure [1]. In this case, two soil layers characterize the soil structure: a top layer of thickness, h, and resistivity, ρ_1, over a layer having resistivity, ρ_2, and considered infinite in depth, as shown in Figure 3.1. The three variables ρ_1 , ρ_2, and h can be determined by interpreting the apparent resistivity values ρa measured using a number of techniques described in detail in IEEE Standard 81 [2], with the Wenner four-pin method perhaps being the most commonly used technique. In brief, four probes are driven into the earth along a straight line, at equal distances apart. The voltage between the two inner (potential) electrodes is then measured and divided by the current between the two outer (current) electrodes to give values of resistance and resistivity, ρ_a.

The formula of multiple images shown in Figure 3.2 is analytical and tedious. Each of its asymptotes, based on the replication of the Sunde's curves, as presented later in Figure 3.3, is a straight line or an exponential curve. The simplicity is vigorous as each asymptote is actually a term in the general solution of the Laplace equation, the partial differential equation that governs the electric static fields. With each asymptote individually derived, the separate asymptotes may be reassembled back into a formula covering the full range of parameters. The re-assembled formula from the asymptotes may be named a "synthetic asymptote." The details of the reassembling are given in the following sections. Synthetic asymptotes are usually quite accurate for monotonically increasing or decreasing functions because they are actually curve fits of the interior points between two asymptotic limits. The synthetic asymptote has recently been successfully used in microwaves (e.g., [20] and [21]).

The tediousness of the multiple images shown also means that it is difficult to extend the Sunde's curves of two-layer soil into that of three-layer soil. On the other hand, the simplicity of

the synthetic asymptotes of the Sunde's curves means that now it may be possible to extend the synthetic asymptote into the three layer soil. When one studies Figure 3.4, one will notice that the addition of one extra layer of soil means that the intermediate asymptote, the circled 2 or 4, simply becomes a little irregular. This change in the intermediate asymptote for a three-layer soil can be studied in further research.

3.1 Images of a Charge in Two-Layer Soils

3.1.1 Images and their reduction to simpler forms for near and far distances along the soil surface

Consider a point source, *I*, shown on the surface of a two-layer soil model in Figure 3.1(a). In Figure 3.1(b), the air-soil boundary is shown reflected, with the air being completely non-conductive. The multiple images of the source, *I*, on the surface of the two-layer soil, and its apparent appearance at small and large distances along the surface, are shown in Figure 3.2.

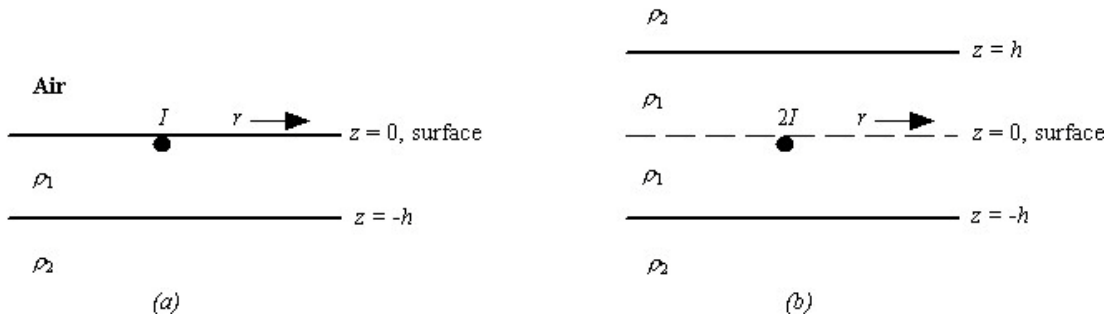

Figure 3.1 The geometry of a point source I in two-layer soil.

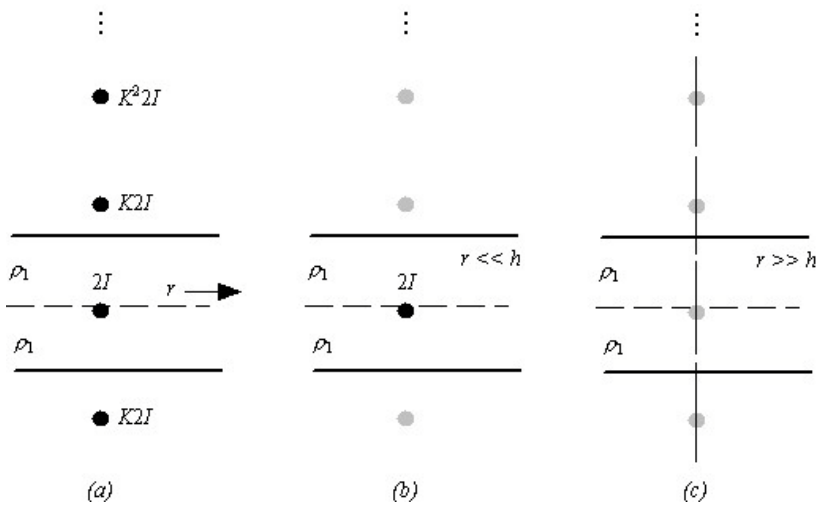

Figure 3.2 The point source, I, and its images as they appear within the top layer. (a) Exact representation. (b) Representation for the near field. (c) Representation for the far field - the point source and all its images are considered as line sources each of length 2h, forming a continuous line of changing current density without changing the far field. The current density along the line section is K^n I/h, where n represents the order of image.

The abrupt change in resistivity at the boundaries of each soil layer is described by means of a reflection factor, *K* [1]:

$$K = \frac{\rho_2 - \rho_1}{\rho_2 + \rho_1} \tag{3.1}$$

Sunde [9] computed and plotted the apparent resistivities along the surface distance using multiple images. The plots are reproduced as Figure 3.3. The apparent resistivity, ρ_a, may be defined from Coulomb's law, i.e.,

$$V = \frac{\rho_a I}{2\pi r} \tag{3.2}$$

With a source point current, *I*, *V* is the measured field point voltage at a distance *r* away on the surface of the two-layer soil. A factor of 2 is used in the denominator of (3.2) instead of 4 because current only flows in the lower half space of soil and not in the upper half space of air. The ρ_a defined in (3.2) agrees with that of Wenner's 4-probe method [2]. Hence, from the measured field point and the input current *I*, the apparent resistivity is

$$\rho_a = rV_a \frac{2\pi}{I} \tag{3.3}$$

This apparent resistivity ρ_a is to be compared to the resistivity of the corresponding apparent voltages V_a and V of the same I to get

$$\frac{\rho_a}{\rho_1} = \frac{V_a}{V_1} = \frac{V_a}{I}\frac{2\pi r}{\rho_1} \tag{3.4}$$

3.1.2 The Asymptotes of Sunde's Curves

The asymptotes of Sunde's curves are sketched in Figure 3.3(b), and it should be noted that the *x*-axis is given by log *r/h*, and the *y*-axis by log ρ_a/ρ_1. In the case of $y = 0$, it corresponds to an asymptote; however, there are 4 asymptotes in two regions. In the first region, *y* is positive, corresponding to the case where $\rho_2 > \rho_1$; in the second region, *y* is negative, corresponding to the case where $\rho_1 > \rho_2$. In the region where $y > 0$ ($\rho_2 > \rho_1$), there are 2 asymptotes, as indicated in Figure 3.3: Asymptote 2 is a straight line section inclined at 45°, going from $x = 0$ to its intersection with the horizontal line of $y = \log \rho a/\rho 1$, for $\rho_1 < \rho_2 < \infty$, and Asymptote 3 is a horizontal section where $y = y_2$ (i.e., $\rho_a = \rho_2$), at $x \rightarrow \infty$ beyond the interception of Asymptote 2. In the region where $y < 0$ ($\rho_2 < \rho_1$), there are 2 asymptotes: Asymptote 4 is an exponential decay section where $y = e^{-Bx}$ between $x = 0$ and the intersection with Asymptote 5, a horizontal section beyond the interception. The constant *B* is derived later in (3.14), but in the log-log form of Figure 3.3(b).

3.1.3 Development of the Asymptotes – The Nearby Field from the Source

On the soil surface with the distance *r* being much smaller than *h*, as indicated in Figure 3.2(b), only the potential from the point source is significant, and the influence of the images can be neglected. The source is completely in the ρ_1 medium, and hence the Laplace solution is trivial, i.e., resulting in Coulomb's law, i.e.,

$$V = \frac{\rho_1 I}{2\pi r} \tag{3.5}$$

This is the same as (3.2), indicating that:

$\log\frac{\rho_a}{\rho_1} = \log 1 = 0$, which is where $y = 0$. (3.6)

This corresponds to asymptote 1 in Figure 3.3(b).

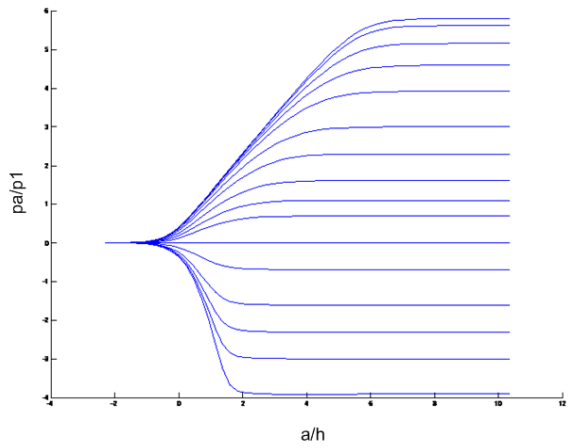

Figure 3.3 (a) Sunde curves for two-layer soil structure from image theory.

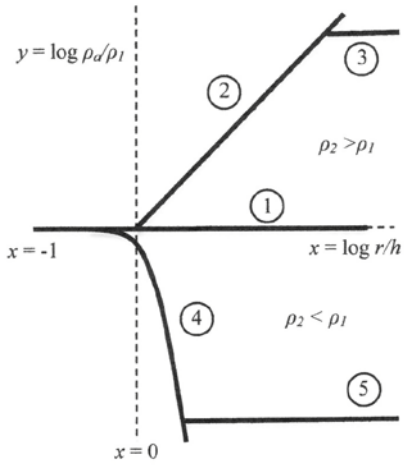

Figure 3.3(b) Asymptotes of the Sunde's curves, with x = log r/h, and y = log ρa/ρ1.

3.1.4 The Far field with *y* > 0

Far from the source, *r* is much larger than *h*, and Figure 3.3(a) can be redrawn as shown in Figure 3.3(b). In this case, the top layer, having thickness *h*, appears to disappear from view so that, corresponding to Figure 3.1(b), the point source, *I*, appears to be in a homogeneous media of ρ_1. Similar to (3.4), Equation 3.7 is obtained:

$$V = \frac{\rho_1 I}{2\pi r} \tag{3.7}$$

This is the same as in (3.2). Equation 3.8 is obtained:

$$\log \frac{\rho_a}{\rho_1} = \log \frac{\rho_2}{\rho_1} = y \tag{3.8}$$

This is the correct asymptote of $x \rightarrow \infty$ in the very far right region in Figure 3.3(b), i.e. asymptotes 3 and 5.

3.1.5 Laplace Solution for the Intermediate Far Field (for 0 < x < the intersection of the asymptote)

The intermediate far field corresponds to asymptotes 2 and 4 in Figure 3.3(b). The 3D structures and fields of the point source and images in Figure 3.2 have circular symmetry around the *z*-axis. The Laplace equation therefore reduces to the following form:

$$/\frac{1}{r}\frac{\partial}{\partial r} r \frac{\partial}{\partial r} V + \frac{\partial^2}{\partial z^2} V = 0 \tag{3.9}$$

The general solution of the above partial differential equation, under the general structure of Figure 3.1 and 3.2, is then

$$V = \rho_1 \frac{(I/h)}{\pi}[B_0 \ln(\frac{r}{h}) + B_1 K_0(\frac{\pi}{2}\frac{r}{h})\cos(\frac{\pi}{2}\frac{z}{h})] \tag{3.10}$$

where B_0 and B_1 are arbitrary constants associated with the general solution to be matched with boundary conditions known in Figure 3.4 [23]. K_0 is the modified Bessel function of zero order, i.e., independent of the azimuth angle, ϕ [22]. This solution is associated with the line structure for the far field of Figure 3.2(c), with the first term associated with the case of $y < 0$ *(i.e.* $\rho_2 > \rho_1$*),* and the second term associated with the case of $y > 0$ *(i.e.* $\rho_2 < \rho_1$*).* The corresponding asymptotes of $y = \log \rho_a/\rho_1$ can now be generated.

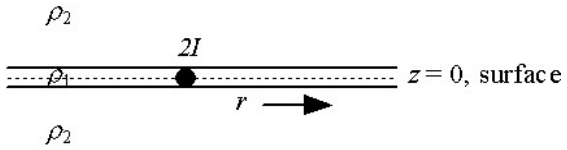

Figure 3.4 The far field, very far from the source.

For asymptote 2, Figure 3.2(c) line structure has the reflection $K = 1$, i.e., infinite length, with a uniform current density of $I/2h$. From the first term of Equation 3.10, we have:

$$V_a = B_0 \frac{I\rho_1}{h\pi}\ln(\frac{r}{h}) \tag{3.11}$$

When substituted into (3), we get:

$$\frac{\rho_a}{\rho_1} = \frac{V_a}{I}\frac{2\pi\, r}{\rho_1} = \frac{2rB_0}{h}\ln(\frac{r}{h}) \tag{3.12}$$

or

$$\log(\frac{\rho_a}{\rho_1}) = \log(\frac{B_0 r}{h}) + \log[\ln(\frac{r}{h})^2] \tag{3.13}$$

i.e., at $r >> h$, but still in the middle range of $y = \log(r/h)$ in Figure 3.4. The second term in (3.13) may be neglected, as the doubled log (i.e., log-ln) function will be very small; then the

first term, after some straightforward manipulation, and in the coordinates of x and y of Figure 3.2(b), becomes:

$$y = \log(\frac{\rho_a}{\rho_1}) = \log(B_0 \frac{r}{h}) = \log(\frac{r}{h}) = x \tag{3.14}$$

where a match with the upper half of Figure 3.4 gives the constant $B_0 \approx 1$. This is the asymptote of the $+45^o$ slope in the upper part of Figure 3.4 (Asymptote 2).

For the intermediate far field with $y < 0$, the Figure 3.2(c) line structure has the reflection $K = -1$, i.e., of infinite length with alternate changing signs of current density of $I/2h$. From the second term of (3.8), i.e. $x >> 0$, on the soil surface of $z = 0$, we have the following approximation [10]:

$$V_a = B_1 \rho_1 \frac{(I/h)}{\pi} K_0(\frac{\pi}{2}\frac{r}{h}) \approx B_1 \frac{(I/h)}{\pi} \sqrt{\frac{\pi}{2}} \frac{\exp(-\frac{\pi}{2}\frac{r}{h})}{\sqrt{\frac{\pi}{2}\frac{r}{h}}} \tag{3.15}$$

When substituted into (3.15), we get:

$$\frac{\rho_a}{\rho_1} = \frac{1}{I}\frac{2\pi\ r}{\rho_1} = B_1 \frac{2r}{h} \frac{\exp(-\frac{\pi}{2}\frac{r}{h})}{\sqrt{\frac{r}{h}}} \tag{3. 16}$$

$$= B_1 \sqrt{\frac{4r}{h}} \exp(-\frac{\pi}{2}\frac{r}{h})$$

or, for $r >> h$,

$$\log(\frac{\rho_a}{\rho_1}) = \log B_1 \sqrt{\frac{4r}{h}} + \log[\exp(-\frac{\pi}{2}\frac{r}{h})]$$

$$= \log B_1 \sqrt{\frac{4r}{h}} + 0.434 \ln[\exp(-\frac{\pi}{2}\frac{r}{h})] \tag{3.17}$$

$$= \log B_1 \sqrt{\frac{4r}{h}} - 0.434(\frac{\pi}{2})(\frac{r}{h})$$

$$\approx \log B_1 \sqrt{\frac{4r}{h}} - 0.682(\frac{r}{h}) \approx -0.682(\frac{r}{h})$$

and hence,

$$y = -0.682 * 10^{x} \tag{3.18}$$

which is asymptote 4, an exponential decay. This equation applies even to the negative values of x, and, as a result, (3.6) is not required when $y_2 < 0$.

3.1.6 Construction of the Synthetic Asymptotes

The synthetic asymptote is a curve-fit between two asymptotes, at the near and the far limits of the parameter concerned. For the case of $y_2 > 0$, we need to synthesize from the asymptotes of (3.6), (3.8) and (3.14). For the case of $y_2 < 0$: we need to synthesize from the asymptotes of only (3.8) and (3.18).

For $y_2 > 0$, we first combine the asymptotes of **(**3.18) and (3.14) as those of a hyperbola, i.e., we let

$$y(y - x) = A \tag{3.19}$$

where A is a constant to be determined by matching with the numerical data of Sunde's curves. (3.16) is a quadratic equation of y of which the solution is simply:

$$y = \frac{x + \sqrt{x^2 + 4A}}{2} \tag{3.20}$$

Then, the synthetic asymptote (3.19) is combined with (3.8), in the form of a p^{th} power norm, to give the final synthetic asymptote:

$$(\frac{1}{y})^p = [\frac{1}{x + \sqrt{(x^2 + 4A)/2}}]^p + [\frac{1}{y_2}]^p \tag{3.21}$$

where $y_2 = \log \rho_2/\rho_1 \geq 0$, $y = \log \rho_a/\rho_1$ and $x = \log r/h$. The constant p was determined by matching it to numerical data. After some investigation, it was found that A could be set to 0.05, and the power, p, to 4 (the specific values of these two constants, and p below, are not critical, and do not play a significant role in the determination of the soil model).

For $y_2 < 0$, the asymptotes of (3.8) and (3.18) can be combined in the form of the p^{th} norm of the reciprocals. The resulting synthetic asymptote is:

$$(\frac{1}{-y})^q = (0.682 * 10^x)^q + (\frac{1}{-y_2})^q \quad (3.22)$$

where, again, $y_2 = \log \rho_2/\rho_1 \leq 0$, $y = \log \rho_a/\rho_1$ and $x = \log r/h$. Note that y and y_2 have changed signs above to ensure $q > 0$. The constant q was determined by matching it to numerical data. After investigation, it was found that q could be set to 2.

Equations 3.21 and 3.22 are the two parts of the full and final formula for Figure 3.4, that is, a part for $y_2 < 0$ and the other for $y_2 > 0$. Corresponding to Figure 3.3 and 3.4, they are for $\rho_2 < \rho_1$ and $\rho_2 > \rho_1$, or, corresponding to (1), they are for the image reflection coefficients of $K < 0$ and $K > 0$. Superposition of the asymptote sections of the synthetic asymptotes of Figure 3.4 onto the actual Sunde's curves of Figure 3.3(a) shows that the asymptote sections agree with the corresponding Sunde's curves very well, except when two asymptotes intercept their direction changes abruptly. To smooth out this abruptness, the constants A, p and q of the synthetic asymptotes Equations 3.21 and 3.22 are included. With a suitable choice of these constants of smoothing, it is clear that the synthetic asymptotes (3.21) and (3.22) can be highly accurate.

3.1.7 Extraction of the Soil Model by Formula

Before numerical examples are presented, the mathematical form of the extraction of the soil model is given. The synthetic asymptotes of both (3.21) for y > 0 and (3.22) for y < 0 have the form of a general function, f, i.e.

$$y = f(x, \rho_1, \rho_2, h) \quad (3.23)$$

or, in a slightly more specific form of a function, ρ_a^c, i.e.,

$$\rho_a^c = f(r_i, \rho_1, \rho_2, h) \quad (3.24)$$

at specific locations r_m along the soil surface of the measured point, m. The constraints of optimization limit ρ_1, h and ρ_2 to non zero values ensures that the optimization process will converge on a solution. However, when either ρ_1 or ρ_2 were less than 1, then the soil model was assumed to be uniform. If the distance of m = 1, 2, 3, N would be a series of measured soil resistivities. The value of ρ_{ai}^m is then obtained in the field at the same locations. A simple penalty function F is then used to find the unknowns of the 2-layer model: ρ_1, h and ρ_2, that is, by

minimizing the mean square error between the predicted/computed and measured resistivity values:

$$\min F = \sum_{i=1}^{N} [\rho_{ri}^{c} - \rho_{ri}^{m}]^2 \tag{3.25}$$

The soil model of ρ_1, h and ρ_2 is obtained when the above function is reduced to a minimum in through optimization. For initial values in the optimization, ρ_1 is set to the average of the lower 10% of the measured apparent resistivity values, ρ_2 to the average of the remaining 90%, and h to depth of 1 meter.

3.2 Results and Discussion

The algorithm was verified using the data in [13] (repeated in Table 3.1) to estimate the soil parameters in two-layer soil without the use of the pre-determined master curves developed in [13]. Table 3.2 shows the excellent results achieved and it can be seen that the results obtained are essentially identical to those found in [13]. Figure 3.5 shows the fit of the model obtained to the actual measured data ρ_a in the field, and, again, the results are excellent – the soil model obtained passes through of all the data points. The difference between the proposed algorithm and the one from [13] is a significant computational savings from the elimination of multiple complex images.

Table 3.1 Soil measurement data (from [13]).

***r* (m)**	**ρ_a (Ω.m)**
2.5	320
5.0	245
7.5	182
10.0	162
12.5	168
15.0	152

Table 3.2 Comparison between proposed Algorithm and Dawalibi.

	Proposed Method	**Dawalibi et al [1]**	**% Difference**
$\boldsymbol{\rho_1}$ **(Ω.m)**	383.54	383.0	0.14
$\boldsymbol{\rho_2}$ **(Ω.m)**	147.68	147.7	0.02
h **(m)**	2.56	2.56	0.09

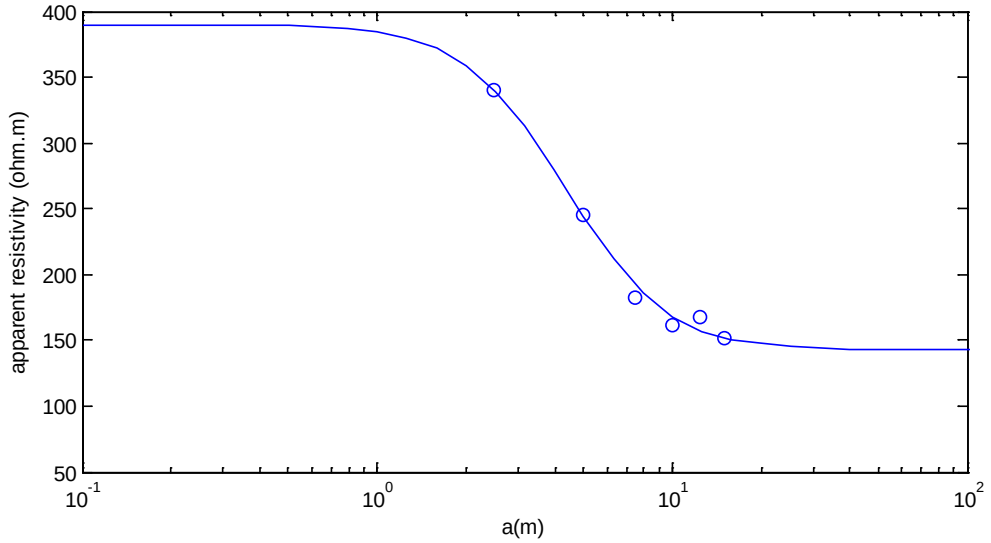

Figure 3.5 Fit of the model to the measured data, ρ_a (measured values are represented by circles).

Gonos and Stathopulos [19] also introduced an error function as a measure of the fit between measured and computed values of soil resistivity to determine a comparison for the various techniques currently used determining the grounding parameters in two-layer soil:

$$F_g = \sum_{i=1}^{N} \frac{\left|\rho_{ri}^m - \rho_{ri}^c\right|}{\rho_{ri}^m} \tag{3.26}$$

Del Almo used Equation 3.26 for a comparison of eight methods currently used. These are summarized as follows and can be reviewed in detail in [18]:

1. Methods proposed IEEE 81-1983 standard which were discussed in Chapter 2.
2. Implementation of EPRI, Report EL 2682 [43] which basically used a first order gradient technique.
3. Improved first order gradient technique, which was quite similar to [45], except a

weighting factor was introduced for the safety parameters themselves.

4. A second order gradient technique was introduced which allowed for faster convergence of the solution space itself.
5. A technique based on Levenberg-Harquart method (LMT).
6. A technique based on the inverse generalized method (IGT).
7. A technique based on Quassi-Newton method (QNT).
8. A technique based on a mixed method (LMT).

All of the eight methods compared by Del Almo are based on image theory which fundamentally slows the speed of determining the grounding grid parameters to the point where researchers have not tackled the overall optimization of the grounding grid itself. The algorithm proposed in Chapter 3 was applied to the examples provided in [17], and the results are shown in Table 3.3, along with a comparison to the results obtained on those same examples in [19]. In addition, the proposed algorithm was also applied to examples provided in [19], and the results are shown in Table 3.4, along with a comparison to the results obtained on those same examples in [19].

Table 3.3 Comparison of the proposed method with the methods of Seedher and Arora [17] and Gonos and Stathopluos [19] (smallest F_g values bolded).

Case	ρ_1 **(Ω.m)**	P_2 **(Ω.m)**	h **(m)**	**Error** F_g	**Method of solution**
1	1000.350	21.140	0.990	1.291	[17]
	1000.003	20.526	1.000	1.275	[19]
	999.781	19.995	1.000	**0.001**	Proposed
2	98.380	1018.800	2.440	0.354	[17]
	98.194	973.609	2.424	0.014	[19]
	96.143	866.431	2.267	**0.038**	Proposed
3	99.990	302.640	5.040	0.005	[17]
	100.762	327.962	5.323	0.002	[19]
	100.000	299.990	5.000	**0.002**	Proposed
4	383.498	147.657	2.563	0.208	[17]
	389.493	152.966	2.403	0.242	[18]
	367.739	143.569	2.708	0.165	[19]
	389.206	145.836	2.332	**0.152**	Proposed

Table 3.4 Comparison of the proposed method with the best method of Del Alamo [18], and Gonos and Stathopulos [19]. (Smallest F_g values bolded)

Case	ρ_1 (Ω.m)	ρ_2 (Ω.m)	h (m)	Error F_g	Method of solution
1	372.729	145.259	2.690	0.1884	[18]
	374.921	144.518	2.559	0.1600	[19]
	362.435	142.665	2.841	**0.1518**	Proposed
2	246.836	1058.62	2.139	0.2126	[18]
	243.419	986.960	2.000	0.1829	[19]
	242.372	983.67	1.982	**0.1798**	Proposed
3	57.343	96.712	1.651	0.4043	[18]
	58.229	91.039	1.310	0.3635	[19]
	57.998	87.636	1.102	**0.3619**	Proposed
4	494.883	93.663	4.370	0.2338	[18]
	499.827	89.847	4.409	0.2029	[19]
	481.064	89.566	4.529	**0.1870**	Proposed
5	160.776	34.074	1.848	0.1852	[18]
	168.694	39.463	1.625	0.1512	[19]
	173.431	46.805	1.389	**0.1409**	Proposed
6	125.526	1093.08	2.713	0.8538	[18]
	128.645	1060.97	2.896	0.2771	[19]
	131.014	961.64	2.456	**0.3373**	Proposed

In comparing the error produced by the method proposed in this chapter with previous methods, it is clear that use of the proposed method provides for an increase in the accuracy of the calculation of parameters of two-layer earth. For the 10 examples examined, in every case except two (Case 2 of Table 3.3, and Case 6 of Table 3.4), the difference between the measured and calculated resistivities is smallest for the method being proposed in this chapter. The proposed method finds a very good solution each time, but clearly not the optimum solution in every case. However, it is apparent that the proposed method does a better job than other algorithms published to date. The concept of optimization for finding soil models, first introduced by Gonos and Stathopulos [19], significantly reduces the errors in the determination of the two-layer soil parameters. When the Sunde's curves are put into analytical form using synthetic asymptotes, the extraction of the soil model becomes automatic and rapid.

3.3 Conclusions

A novel method was developed in this chapter to help eliminate the usual practice of using a set of resistivity curves to generate the model of a two layer soil directly from field measurements. The data manipulation, the approximations and optimization for accuracy, with manual steps, have typically been complicated for the engineer involved. The set of resistivity curves is from the Sunde's curves of two-layer soil (Figure 2.7) generated by multiple reflection images between soil layers. The multiple reflections cause the analysis of the resistivity curves to be inherently tedious. The method proposed in this chapter overcomes this challenge by looking at the asymptotes of the two-layer soil, some by simple inspection of the geometry, and some by analytical asymptotic expansions of the general solutions of the Laplace equation. The resulting asymptotes therefore are both vigorous and simple in their mathematical form.

An asymptote is applicable only towards one asymptotic limit. Therefore, one needs to combine two opposite asymptotes, one for each limit of the parameter concerned, into one expression, the synthetic asymptote. The resulting synthetic asymptote is then just as rigorous, and nearly as simple, but is now applicable to both limits. The combination techniques used in Chapter 3 are the asymptotes of a hyperbola and the p^{th} power norm of the function space with an arbitrary constant (such as A, p or q discussed earlier in this chapter) to ensure high accuracy for the two simple synthetic asymptotes, (3.3) and (3.4), of the Sunde's curves.

With the simple and rigorous expressions of the Sunde's curves, the extraction of the soil model of the two-layer soil is now very simple and automatic when run as a computer program. As shown in Tables 3.3 and 3.4, the accuracy is high. Finally, the computation time required for other methods ([13], [17] and [19]), as well as the asymptotic approximation of Chapter 3, are all very small. The main advantage of the asymptotic approximation here lies in its analytical simplicity, that is, as compared to other software in which the complexity of the multiple image and numerical approach. This simplicity gives clear insights and indicates that it should be possible in the future to modify the one asymptote in the intermediate transition region to extend the asymptote approach to three layer soil, or even to multilayer soil; the computing routine should remain fast.

Chapter 4 Grounding System Design Equations

4.0 Introduction

A soil model was developed in Chapter 3. The chapter continues with the grounding system design by outlining how the station grounding resistance is determined. This station grounding resistance is one of the key parameters in substation station design, and can be calculated using numerical techniques. These techniques are widely used to solve electromagnetic field problems that are too complex to be solved by analytical methods alone. To this end, several researchers chose to develop a significant electrostatic modeling and analysis capability based on the *Method of Moments,* as described by Harrington [23], and to be described in detail shortly

This thesis further develops one such method developed by Chow *et al* [24 - 27], who computed the station grounding resistance by expanding on the work of Harrington, and who were the first to introduce the *Galerkin Moment Method* for the computation of grounding grid resistance. This method reduces a set of equations to matrix equations that can be solved numerically through matrix inversion.

With the *Method of Moments,* it was difficult to ensure that voltage boundary conditions were satisfied, and this is the fundamental basis of using the method of image charge, which will be discussed in further detail. The name, "*Method of Moments*," originates from the replacement of certain elements in the original layout with imaginary charges, which replicate the boundary conditions of the problem. As the total electrostatic potential is equal to scalar sum of the potentials, at any point on the *xz* plane, the potential of any real charge will cancel with that of its image, as discussed in Chapter 3. Hence the potential anywhere on the plane will be zero, and the boundary condition is satisfied. Thus, if a voltage, *V,* is applied across a grounding rod, current will flow from the rod into the soil, and the resistance can be calculated. The difficulty discovered was that the applied voltage, *V,* had to be constant in order to maintain the boundary condition required for electrostatic image theory; however, there will be some leakage current associated with that voltage drop. To this end, the current density has to be simulated to be constant along the rod segment to use Chow *et al's* method. This chapter introduces a new method of handling the equipotential boundary condition requirements.

4.1 Background on Previous Works

In an early work by Dwight [28], an equation was developed for calculating the ground resistance for different the shape and size of different electrodes. This equation was based on the duality concept between the DC resistance to ground of a conductor and its capacitance. Dwight's equation is a rough approximation and is limited to uniform soil models and is given by:

$$R = \frac{\rho}{4}\sqrt{\frac{\pi}{A}} \tag{4.1}$$

where ρ is the resistivity of soil, Ω-m

A is the area of the grounding grid, m

Equation 4.1 only considers the area of the grounding grid itself and does not take into account any of the conductors within this area. Laurent and Nieman [29, 30] expanded Equation 4.1 to take into account the actual total length of conductors, and their equation was made part of the IEEE standard. The equation is:

$$R = \frac{\rho}{4}\sqrt{\frac{\pi}{A}} + \frac{\rho}{L} \tag{4.2}$$

where ρ is the resistivity of soil, Ω-m

A is the area of the grounding grid, m^2

L is the total length of grounding conductor, m

The next development came from Nahman and Salamon [31], who introduced correction factors for the non-uniform current density over the corners of the meshes of a grid. Nahman and Salamon gave a better approximation than Equation 4.1; however, these corrections factors were not rigorously generated, and, in addition, the equation was still limited to uniform soil. The equation did take into account the conductor spacing and the number of conductors in both the horizontal and vertical directions, and is given by:

$$R = \rho\left(\frac{0.53}{\sqrt{A}} + \frac{1.75}{Ln^{\frac{1}{2}}}\right)\left(1 - 0.8\frac{100hd}{n\sqrt{A}}\right)\frac{1}{4} \tag{4.3}$$

where ρ is the resistivity of soil, Ω-m

A is the area of the grounding grid, m^2

L is the total length of grounding conductor, m

n number of grid conductors in one direction

d is the diameter of the grid conductors, m

h is the depth of the grounding grid, m

The next advancement in the determination of the grounding resistance came from a paper by Schwartz [3], where constants were introduced based on the grounding grid geometry. Equation 4.4 shows the introduction of geometry corrections, and this method was also adopted in the IEEE standard [1].

$$R = \frac{\rho}{\pi L}\left[ln\left(\frac{2L}{h'}\right) + K_1\left(\frac{L}{\sqrt{A}}\right) - K_2\right] \quad (4.4)$$

where ρ is the resistivity of soil, Ω-m

A is the area of the grounding grid, meters^2

L is the total length of grounding conductor, meters

h' =sqrt(*dh*) for the conductor buried at depth *h*, meters

d is the diameter of the grid conductors, meter

K_1 =-0.04W+1.41 for *h*=0

K_1=-0.05W+1.12 for *h*=1/10*sqrt(Area)

K_1=-0.05W+1.13 for *h*=1/6*sqrt(Area)

W= length/width of the grid

K_2 =-0.15W+5.5 for *h*=0

K_2=-0.10W+4.68 for *h*=1/10*sqrt(Area)

K_2=-0.05W+4.4 for *h*=1/6*sqrt(Area)

There were a few other advancements that extended the research to two-layer soil models [32- 39], but they never solved the problem of uniform current. To resolve the last outstanding issues, Chow *et al* [27] used the *Galerkin Moment Method* and introduced compensating spheres. In the previous papers by Chow *et al* [24 - 27], parallel conductors (representing rodbeds) were considered, and with two conductors having any orientation in a homogeneous or two layer earth, allowing the study of a realistic grounding system, where driven rods are connected to the grounding grid. The advantage of applying the Galerkin's approach is its usefulness for bigger grounding systems, where the size and the number of conductors are large. Due to the assumption of uniform outward current density in each conductor imposed by the *Galerkin's Moment Method*, this technique does not entirely satisfy the equipotential boundary condition

along a driven conductor or in a grid well. For accurate calculation of the surface potential, the boundary conditions must be satisfied.

The next part discusses the fundamental basis of the work developed by Chow *et al* in the introduction of the *Galerkin Moment Method*, with the introduction of the spheres to correct current boundary conditions.

4. 2 Galerkin's Moment Method

The *Galerkin Moment Method* reduces functional equations to matrix equations that can be solved numerically through matrix inversion to provide a procedure for solving linear equations. The *Galerkin Moment Method* uses a set of weighted residuals developed through the following equations. The objective is to approximate the solution to an operator equation:

$$L(f) = g \tag{4.5}$$

where L represents a linear operator,

g is a known function (i.e., electric field), and

f represents the unknown function (i.e., the current).

In the case where f is the unknown function (the current), it can be determined, and the method of moments represents the unknown, f , by a set of functions (f_1, f_2, f_3,…) as a linear combination:

$$f = \sum_n \alpha_n f_n \tag{4.6}$$

where α_n are constants to be determined by the f_n , known as base, or expansion, functions which are arbitrarily selected. By substituting Equation 4.5 into Equation 4.6, and using the linearity of L, the following summation is derived:

$$g = \sum_n \alpha_n L f_n \tag{4.7}$$

Equation 4.7 has N unknowns and it is necessary to have N independent linear equations, which are obtained by taking the inner product of Equation 4.7 with another set of functions, named weight functions, in the L domain, giving:

$$\sum_n \alpha_n \langle w_m, L f_n \rangle = \langle w_m, g \rangle \tag{4.8}$$

where m =1,2,3... in the range of L. The inner product will be an integral of area of the two functions, and Equation 4.8 can be written in matrix form as:

$$[\langle w_m, L f_n \rangle][\alpha_n] = [\langle w_m, g \rangle] \tag{4.9}$$

where $[l_{mn}][\alpha_n] = [g_m]$.

If the inverse of [*l*] exists, the constants (α_n) are obtained by Equation 4.10:

$$[\alpha_n] = [l]^{-1}[\langle w_m, g \rangle] \tag{4.10}$$

and a solution for *f* exists.

By comparing Equation 4.9 and Equation 4.5, and using the linearity operator, an equation can be obtained relating impedance, voltage and current:

$$[Z_{mn}][I_n] = [v_m] \tag{4.11}$$

where $[Z_{mn}]$ and $[V_m]$ are known as impedance and voltage matrices and will be used later within this Chapter.

The solution may be exact or approximate depending on the choice of f_n and w_n. This is known as Galerkin's Moment Method when f_n and w_n are taken to be the same values. An example is provided to show the method.

Let $g(x) = 1+4x^2$, and find $f(x)$ in the interval $0 \leq x \leq 1$ (note that this example comes from Harrington [16]:

$$\frac{-d^2 f}{dx^2} = 1 + 4x^2 \tag{4.12}$$

and $f(0) = f(1) = 0$,

This has a solution, $f(x) = \frac{5x}{6} - \frac{x^2}{2} - \frac{x^4}{3}$

If one chooses $f_n = x - x^{n+1}$ for n = 1, 2, 3, N, the series from Equation 4.6 is represented by Equation 4:13.

$$f = \sum_{n=1}^{N} \alpha_n (x - x^{n+1}) \tag{4.13}$$

It should be noted that the term, "*x,*" is needed in Equation 4.13, otherwise f_n, will not be in the domain of *L*, meaning that the boundary condition will not be satisfied. Equation 4.14 is used to make the form Galerkin:

$$w_n = f_n = x - x^{n+1} \tag{4.14}$$

Evaluation of the matrices of 4.9 with $L=-d^2/dx^2$ results in the following solution:

$$l_{nm} = \langle w_m, Lf_n \rangle \tag{4.15}$$

$$\int_0^1 (x - x^{n+1}) \frac{d^2}{dx^2} (x - x^{x+1}) dx$$

$$= \frac{mn}{m + n + 1}$$

and

$$g_{nm} = \langle w_m, g \rangle = \frac{m(3m + 8)}{2(m + 2)(m + 4)} \tag{4.16}$$

For any fixed value of N (number of expansion functions), the constants (α_n) are given by Equation 4.10 and the approximation to f by Equation 4.15. In order to illustrate the Galerkin method, three different values of N will be demonstrated. For N =1, l_{11} =1/3, g_1=11/30, and α_1=11/10. For N=2, the matrix equation becomes the following:

$$\begin{bmatrix} 1/3 & 1/2 \\ 1/2 & 4/5 \end{bmatrix} \begin{bmatrix} \alpha_1 \\ \alpha_2 \end{bmatrix} = \begin{bmatrix} 11/30 \\ 7/12 \end{bmatrix} \tag{4.17}$$

This yields 1/10 and 2/3 for α_1, and α_2, respectively. In order to obtain the exact solution, a value of N=3 yields the following:

$$\begin{bmatrix} 1/3 & 1/2 & 3/5 \\ 1/2 & 4/5 & 1 \\ 3/5 & 1 & 9/7 \end{bmatrix} \begin{bmatrix} \alpha_1 \\ \alpha_2 \\ \alpha_3 \end{bmatrix} = \begin{bmatrix} 11/30 \\ 7/12 \\ 51/71 \end{bmatrix} \tag{4.18}$$

This yields 1/10, 0, and 1 for α_1, α_2, *and* α_3, respectively, which is sufficient to reproduce f exactly as shown in Figure 4.1. Figure 4.1 shows the results from N equal to 1, 2 and 3 where the blue curve is N=1, and the red curve is with N equal to 2 and the green curve is the exact solution (N≥3).

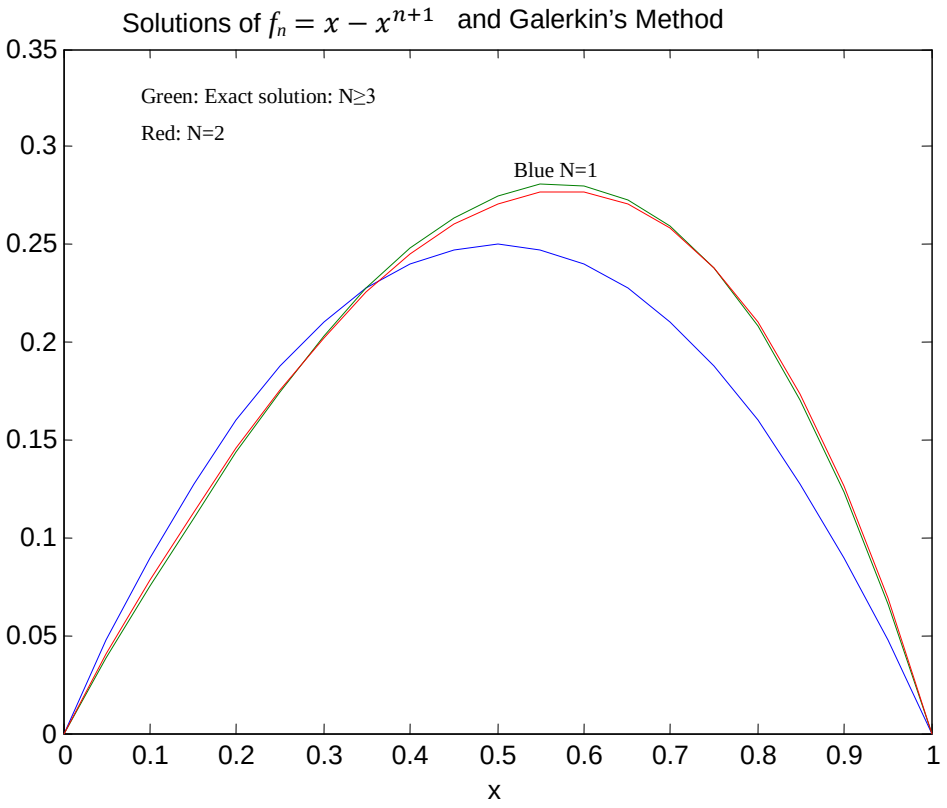

Figure 4.1 Solutions for fn=x-x$^{(n+1)}$.

The next part of this chapter introduces how the *Galerkin Moment Method* was introduced in grounding system design.

4.2.1 Homogeneous Medium - Resistance from a Rod of Uniform Current

Numerical analysis techniques are widely used today to solve electromagnetic field problems that are too complex to be solved by analytical methods alone. For this thesis, a significant electrostatic modeling and analysis capability based on the *Method of Moments,* as described by Harrington [23], was used. Unlike the more popular finite-element approach, one does not solve for fields directly, but rather for the field sources, or in the case here, the charge distribution. Once the field sources have been determined, the fields can be readily computed as needed, using the *Principle of Superposition* [40]. In order to compute the field sources, the governing differential equations (Laplace or Poisson equations) are transformed into integral identities, which are applied to a finite number of elements that form the boundary surfaces of the field problem. A system of linear equations is defined that satisfies the boundary conditions at each

element. In general, the coefficient matrix associated with the resulting system of equations is dense, non-symmetric, and not diagonally dominant, so direct linear system solvers must be used.

As applied to electrostatic boundary-value problems, this method is summarized as follows. In a region of constant permittivity ε and a volume charge distribution $\rho(x,y,z)$, the electrostatic potential $\emptyset(x,y,z)$ satisfies the Poisson equation:

$$-\varepsilon\nabla^2\emptyset(\mathrm{x},\mathrm{y},\mathrm{z}) = \rho(\mathrm{x},\mathrm{y},\mathrm{z}) \tag{4.19}$$

Dirichlet boundary conditions are those conditions for which the scalar potential is specified at every point on the conductor-dielectric boundary and, under these conditions, the unique solution to this problem is defined by Equation 4.20:

$$\emptyset(x'y'z') = \frac{1}{4\pi\varepsilon}\int x\int y\int z\frac{\rho(x,y,z)}{r(x,y,z)}dxdydz \tag{4.20}$$

where *r* is the distance between the source point *(x,y,z)* and the field point *(x'y'z'):*

$$r(x,y,z,) = \sqrt{(x-x')^2+(y-y')^2+(z-z')^2} \tag{4.21}$$

In general, Equation 4.21 cannot be solved at every point on the boundary surfaces; however, if the boundaries are divided into *N* elements, then each element can be defined by a linear equation [16]:

$$\frac{1}{4\pi\varepsilon}\sum_{m=1}^{N} a_{nm}\rho_{m=V_n} \qquad n = 1,2,\ldots N \tag{4.22}$$

In this way, the problem becomes an "inverse capacitance density" matrix and the coefficients describe the mutual coupling between the elements, and are defined in terms of the size and orientation of each element relative to the others:

$$a_{mn} = \oint\frac{1}{r(x,y,z)}dm \tag{4.23}$$

where the field point *(x', y', z')* in the function *r* is chosen to be the centroid element, *n*, and the integration is carried over the element, *m*. The potential vector *V* specifies the Dirichlet boundary conditions over the boundary surfaces. The elements of the solution vector ρ_n are the modeled charge densities for each element. Generally, it is necessary to model charged objects as equipotential surfaces. This does not mean that these objects are "good" conductors only that the charge relaxation time (i.e., the time needed to redistribute any charge to the steady-state conditions) is small, compared to the time associated with any changes in the specified boundary

conditions by solving quasi-static boundary-value problems. Time-varying boundary conditions can be modeled with a time-series of quasi-static models, up to the frequency at which these assumptions are no longer valid. This upper frequency limit is dependent on the size and conductivity of the objects being modeled, and on the rate of change of the boundary conditions.

To this end, to simplify Harrington's solution, the Galerkin's moment method of rapid conversion was introduced in [25] for grounding resistance of driven rodbeds. Figure 4.2 (a) shows two parallel rods can be split into any number of segments, where $n \neq m$ for the mutual resistances and Figure 4.2(b) shows one individual segment where $m=n$ for the self resistances. The determination of the number of segments has been well explored [24, 25, 26].

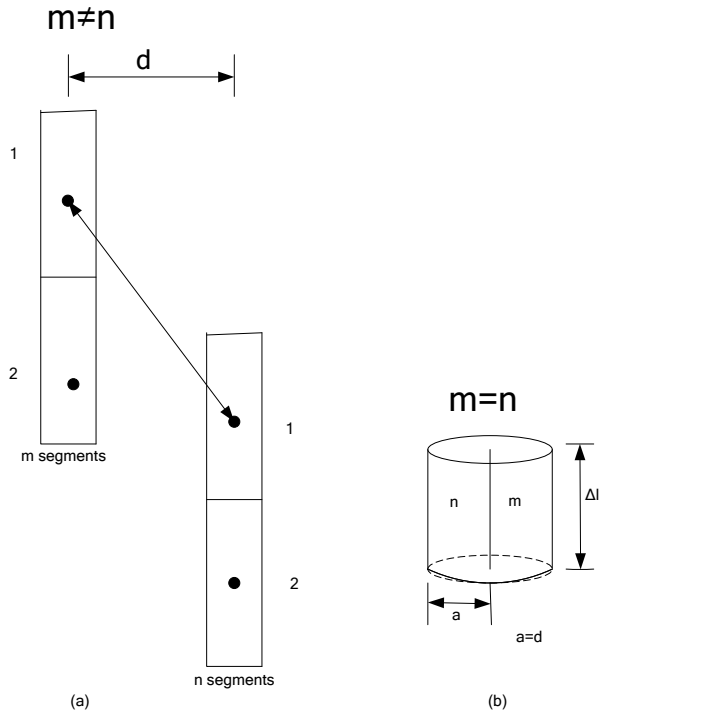

Figure 4.2 Two adjacent conductors segment view.

For any two rods, shown in Figure 4.2, of potentials V_1 and V_2 with assumed uniform current distribution in each rod, I_1 and I_2 in a homogenous medium, the resistance matrix equation can be represented by Equation 4.24:

$$\begin{bmatrix} V_1 \\ V_2 \end{bmatrix} = \begin{bmatrix} R_{11} & R_{12} \\ R_{21} & R_{22} \end{bmatrix} \begin{bmatrix} I_1 \\ I_2 \end{bmatrix} \tag{4.24}$$

where the self ($m=n$) and mutual resistances ($m \neq n$) are represented by Equation 4.25.

$$R_{mn} = \frac{\rho}{I_m I_n} \int J_m(l_m) \left[\int J_n(l_n) G(\vec{r}) dl_n \right] dl_n \tag{4.25}$$

and

$$G(\vec{r}) = \frac{1}{|\overrightarrow{r_m} - \overrightarrow{r_n}|} \tag{4.26}$$

is the Green's function and *m, n = 1 or 2*.

For the parallel rods shown in Figure 4.2, the resistance *R* has been analytically determined [7], including the case of *m=n*, the self term, as shown in Equation 4.18. This equation can be extended to any number of rods as shown in Equation 4.21. The derivation of Equation 4.21 stems from the Method of Moments. As explained earlier, the conducting surface is divided into segments, where the current, I_i, is diffused in each segment, and the relationship between each segment voltage and current is given by Equation 4.27 [26]:

$$\begin{bmatrix} V_1 \\ \cdots \\ V_N \end{bmatrix} = \begin{bmatrix} R_{11} & \cdots & R_{1N} \\ \vdots & \ddots & \vdots \\ R_{N1} & \cdots & R_{NN} \end{bmatrix} \begin{bmatrix} I_1 \\ \vdots \\ I_N \end{bmatrix} \tag{4.27}$$

where I_i, is the current of segment *i* (i = 1,2, ...,*N*), V_i is the voltage of the segment *i* (i = 1,2, ...,*N*), and R_{nm} is the resistance between segment *n* and segment number *m*.

Chow *et al* demonstrated that a reduced number of segments introduced errors in the calculation of the resistance of the grounding grid [26]. By extending their work, this research split each horizontal conductor and vertical ground rod into 2 segments. Therefore, for any two rods as shown in Figure 4.2, there are two segments, one for rod 1 and the other for rod 2. With two segments, each segment will have a self term and there will be two mutual terms between them. It is analytically proven [26] that the error reduction property of each Galerkin's term in Equation 4.27 remains intact regardless of the orientation of the two rods to each other, which means that the *Galerkin's Moment Method* can be applied to grids as well as grid to rod. Each conductor along the whole length of grid is considered as a rod of uniform current distribution, and there are mutual resistances *R* between perpendicular rods, as shown in Figure 4.2.

4.2.2 Homogeneous Medium - Equipotential on Boundaries by Adding Spherical Segments

Galerkin's moment method gives rapid convergence to the grounding resistance of grids and rods, but the uniform current distribution assumed in the method does not satisfy the equipotential boundary condition along a rod, driven, or in a grid. Figure 4.3 shows that the assumption of uniform current distribution along the rod gives large deviations from uniform potential (blue line) at the tips of the rod (red line). In the works of Chow *et al*, the deviation was corrected to some extent by shortening the rod segment, putting a spherical segment of the same radius of the rod itself at the tip and re-matching the boundary condition of constant potential there. The change in potential as a result of this correction is shown in Figure 4.3 (green curve). After a distance of 8 meters, the deviation from the normalized boundary voltage is almost 40%, and this was reduced to 20% with the spheres.

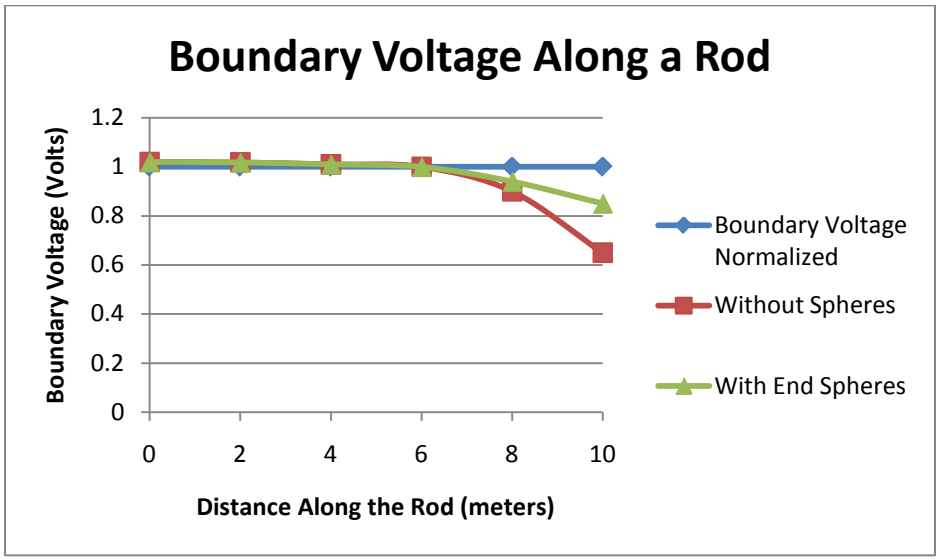

Figure 4.3 Boundary voltages along a rod.

4.2.2.1 Introduction of Modified Sphere Application

To exploit the characteristics of the Simpson's 3 point rule, a rod segment can be represented by three spheres of radii (r_{aa}, r_{bb}, r_{cc}), located respectively and exactly at one end of the rod, the midpoint and the other end of the rod. Figure 4.4 shows how a rod is represented by three spheres.

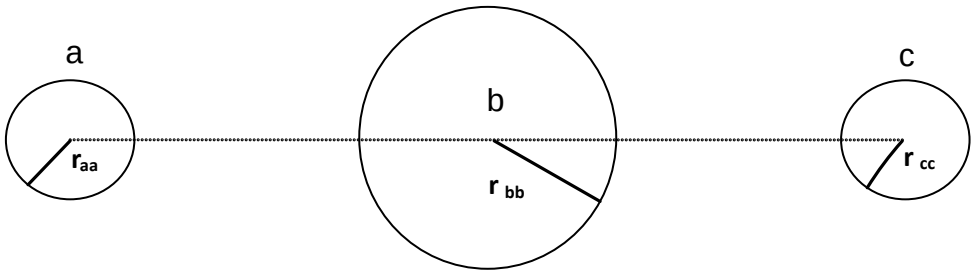

Figure 4.4 Rod represented by three spheres.

In Figure 4.4, the rod of length l is converted into 3 spheres a, b and c to calculate the capacitance in the MoM computations to determine the resistance of the entire grid. For thin rods, Simpson's rule makes the radius r_{bb} of the center sphere to be asymptotically 4 times the radii of both r_{aa} and r_{cc}, the radii of the 2 equal small spheres. Based on the assumption that a rod extends from $-l/2$ to $l/2$ having radius a and linear charge ρ_1 coul/m, the voltage V at a field point, (x) is given by Coulomb's Law [41]:

$$V(x,y) = \frac{1}{4\pi\varepsilon_o}\int_{-l/2}^{l/2} \frac{\rho_1}{\sqrt{(x-x')^2+y^2}}\,dx' \tag{4.28}$$

For rods where a/l is small (typical for most rods), the authors of [25, 26] demonstrated that the self terms in the MoM equation will be significantly larger than the mutual terms, which results in charge ρ_1 being a constant over the length of the rod. Taking ρ_1 as constant and moving it out of the integral sign in Equation 4.28, by Simpson's rule, Equation 4.28 can be written as:

$$V(x,y) = \frac{\rho_1}{4\pi\varepsilon_o}\frac{1}{6}\left[\frac{1}{\sqrt{(x-\frac{l}{2})^2+y^2}} + \frac{4}{\sqrt{x^2+y^2}} + \frac{1}{\sqrt{(x+\frac{l}{2})^2+y^2}}\right] \tag{4.29}$$

The first term in Equation (4.27) is considered a point charge of $Q_a = p/6$ at one end of the rod, and the second term as a point charge of $Q_b = 4\rho/6$ at midpoint of the rod and the third term as a point charge c of $Q_c = \rho/6$ at the other end of the rod. The middle term of equation 4.31 will diverge near a Simpson's match point when $y = 0$ with $x \sim -l/2$, 0 *or* $l/2$, and, when this term approaches divergence, it can be considered as the large self term. The self term can be considered the capacitance of a sphere of 4 times the radius of the end spheres. The other 2 end terms of Equation 4.29 are mutual terms, and are relatively small in comparison. To solve Equation 4.31, it is necessary to alter the form to matrix format shown in Equation 4.30:

$$\begin{pmatrix} Vo \\ Vo \\ Vo \end{pmatrix} = \frac{1}{4\pi\varepsilon} \begin{bmatrix} 1/r_{aa} & 1/r_{ab} & 1/r_{ac} \\ 1/r_{ba} & 1/r_{bb} & 1/r_{bc} \\ 1/r_{ca} & 1/r_{cb} & 1/r_{cc} \end{bmatrix} \begin{pmatrix} Q_a \\ Q_b \\ Q_c \end{pmatrix} \tag{4.30}$$

where $r_{aa,}$ r_{bb} and r_{cc} are the unknown radii of the three spheres. The non-diagonal components of the matrix are the distance between points *a*, *b* and *c*, i.e. *1/2* or *l*. The total charge can be represented by the following equation.

$$Q_o = Q_a + Q_b + Q_c \tag{4.31}$$

while the capacitance of the rod can be represented by the following equation:

$$C = \frac{Q_o}{V_o} \tag{4.32}$$

The capacitance *C* is known by the integration of Equation 4.32 having a uniform charge from a given V_o. The charges Q_a, Q_b, and Q_c are known from Equation 4.31, and the radii can be solved for r_{aa}, $r_{bb,}$ and $r_{cc.}$ From Equations 4.22-32, the rod is converted into spheres. By changing ε into 1/ρ, *Q* becomes the current, *I*, and the capacitance *C* becomes *1/R*, the grid resistance.

To validate the proposed sphere segmentation method, it was compared to existing work, and the results are shown in Figure 4.5, which compares the boundary voltage along the conducting surface for each segment for the various methods used in the determination of the resistance of each segment. It can be seen that the approach developed as part of this thesis ("Gilbert") comes very close to providing a uniform voltage along the entire length of a rod in a more systemic way.

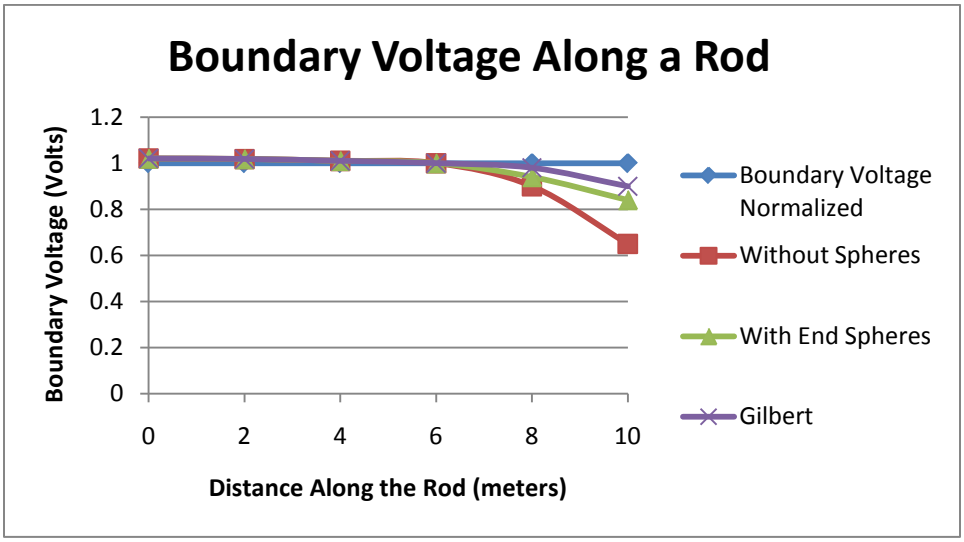

Figure 4.5 Boundary voltages along a rod.

4.3 Procedure Requirements in the Determination of the Grounding Resistance

In Chapter 3, the resistivities of the soil were determined for uniform or two layer soil models. When the model was not uniform in nature, the following parameters were determined: ρ_1 and $\rho_{2,}$ and the depth of the first layer. Simpson's Rule of integration can be used to determine the grounding resistance using a weighted combination of the trapezoidal and midpoint rules of integration. For a two-layer soil structure having ρ_1, ρ_2 with depth $h_{1,}$ (which are used in the development of the image equations discussed in Chapter 3), the trapezoidal rule was used from [23]. Now solving 4.32, the trapezoidal grid resistance, R_{Trap}, Equation 4.33 is used.

$$\begin{pmatrix} V_1 \\ V_2 \\ \vdots \\ V_N \end{pmatrix} = \begin{bmatrix} R_{11} & R_{12} & \cdots & R_{1N} \\ R_{21} & R_{22} & & \\ & & \ddots & \\ R_{N1} & & & R_{NN} \end{bmatrix} \begin{pmatrix} I_1 \\ I_2 \\ \vdots \\ I_N \end{pmatrix} \tag{4.33}$$

This is done to point match the capacitance of the three spheres to determine the radius requirements of the spheres. Again, this is similar to the determination of the solution discussed in [23]. R_{Trap} can be determined from Equation 4.34.

$$R_{Trap} = \frac{V_0}{\sum I_n} \tag{4.34}$$

The second part of the grounding grid resistance solution needs to be determined. For each branch of the grounding grid, it is necessary to find branch n and mid-point radius r_m . At each node of the grounding grid, a node number m versus radii of the mid-point rule r_m and their locations (x, y, z) are determined. With this, the mid-point MoM matrix (MxM) is determined with the required images and is solved to get the mid-point grid resistance $R_{Midpoint}$. To this end, the same matrix solution as Equation 4.33 is used to determine using the midpoint rule of integration to find the mid-point grid resistance $R_{Midpoint}$. With the two values of resistance determined, the Simpson's Rule becomes a combination of the trapezoidal and mid-point rules for much smaller error [42], i.e.,

$$R_{Simspons} = \frac{1}{3}(2R_{Trap} + R_{Midpoint}) \tag{4.35}$$

4.4 Result of the Proposed Modified Sphere Method

With a rod segment represented by three spheres, it was seen in the last section that the deviation from the normalized boundary voltage was reduced to less than 10%, resulting in errors in resistance of less than 1% of that of the end spheres method, as seen in Table 4.1, which compares the resistances of the different grounding systems from the fast Galerkin's moment method and from the point-matched regular moment method of [26] to the method developed in [38]. The dots in each of the case studies shown in Table 4.1 at the intersections of the grounding conductors represent grounding grids, whereas, the dot within the center of any mesh represents where the fault is introduced into the grounding grid itself. As expected the agreement is very good with mean deviations of 1% for resistance with the proposed method. The main advantages of the proposed method are a simplified approach and increased accuracy due to the ability of this method to hold the boundary voltage closer to being constant.

Chow and Salama compared the performance of their equations with other researchers [5], using EPRI computerized results from various studies found in [43] as a baseline reference to check the accuracy of all other formulas. The EPRI report was an in-depth analysis of substation grounding techniques that analyzed various authors' techniques and compared them to field measurements of grounding grids. The grid area used as a basis of comparison was 20m x 20m, the number of meshes in each direction was four, and the conductor diameter of the grid was 0.01m. In [5], Chow and Salama demonstrated their method was the best method for calculating resistance. Figure 4.6 shows the calculated resistances of a substation grounding grid buried at different depths in the soil as a comparison between [5] along with the method presented in this chapter (labeled, "Gilbert"). It can be seen that the proposed method is an improvement upon the method of Chow and Salama.

Table 4.1 Comparison of present results and the available results from reference [26].

Configuration	K	Proposed Method R (Ω)	Ref [26] R (Ω)	Ref [38] R (Ω)
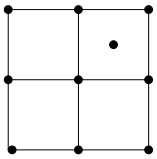	0.9	7.62	7.78	7.78
	0.5	3.31	3.38	3.5
	0.0	1.73	1.77	1.81
	-0.5	0.79	0.81	---
	-0.9	0.16	0.16	0.16
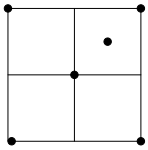	0.9	7.62	7.8	---
	0.5	3.31	3.4	---
	0.0	1.73	1.8	---
	-0.5	0.79	0.84	---
	-0.9	0.16	0.17	---
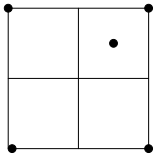	0.9	7.62	7.96	---
	0.5	3.51	3.6	---
	0.0	2.03	2.01	---
	-0.5	1.02	1.05	---
	-0.9	0.26	0.25	---
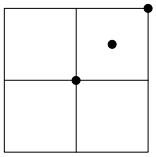	0.9	8.18	8.28	---
	0.5	3.81	3.89	---
	0.0	2.29	2.30	2.28
	-0.5	1.33	1.35	---
	-0.9	0.41	0.42	---
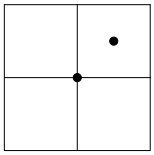	0.9	8.38	8.4	---
	0.5	4.01	4.08	---
	0.0	2.38	2.55	---
	-0.5	1.79	1.79	---
	-0.9	1.29	1.39	---

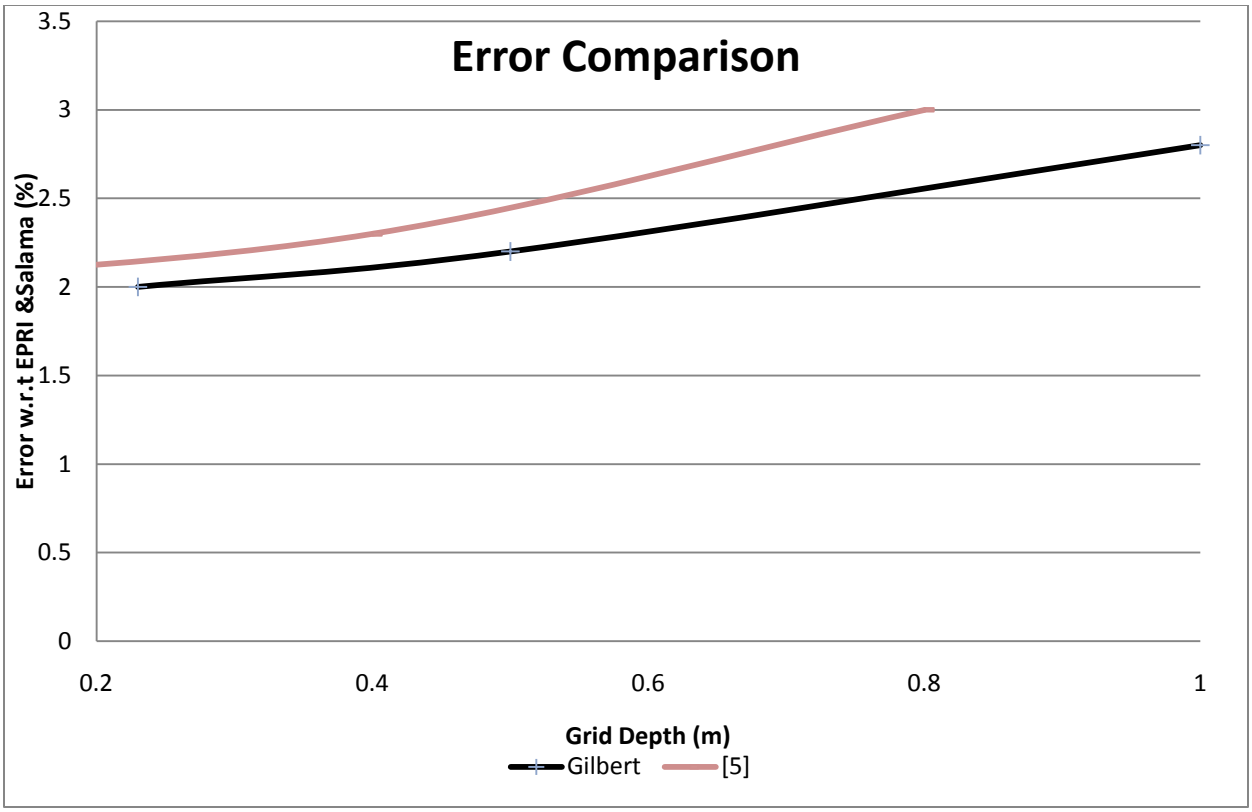

Figure 4.6 Error in the Determination of R_g

4.5 Summary

This chapter provided the specific numerical formulations required to determine the grounding grid resistance. The authors in [26] introduced spheres to improve the boundary conditions; however, the shortcoming of their approach was that it required designer intervention to add spheres at the end. As part of the work for this thesis, a new method was introduced to provide a more systematic approach for sphere placement. The method also reduces errors in calculating the resistance. The method is based on Simpson's rule of integration. The next chapter will use these equations to develop an optimization model for grounding grids in electrical substations.

Chapter 5 Optimization of the Grounding Grid

5.0 Introduction

A grounding system is on one of the most important points inside transmission and power distribution systems. Poor design methods and simplified calculations can lead to high construction costs and unsafe conditions. This chapter introduces a method to design a grounding grid while minimizing time and cost of construction. In this work, computer software has been developed using the equations developed in the previous chapters to solve the *optimization problem* that considers the parameters of a grounding grid, including geometry, depth, conductor size and the number of grounding rods.

The problem is formulated as a mixed integer linear optimization problem. The method incorporates the variables that define the grid characteristics of all possible configurations, including the grid geometry, grid depth, conductor size, and number of grounding rods, size of grounding rods, and, lastly, excavation and installation costs. The optimization problem is subject to safety constraints related to the maximum allowed ground potential rise (GPR), touch and step voltages. The method determines the optimum grid from several possible configurations, so that is a very useful tool for engineering design. A novel optimization technique using a random walk technique to find an optimized grounding grid in a two-layer soil model is proposed. Several examples prove the efficacy of the method.

5.1 Background Information

5.1.1 Optimization of High Voltage Substation Grids

The concept of optimization of a grounding grid has been the focus over the years by researchers who attempted to reduce the amount of copper placed into the earth to form the grounding system design without compromising electrical safety. In [14], the authors first introduced the concept of optimal design of a grounding grid in a two layer soil structure. They verified a new analytical method of soil modeling by comparing predicted and actual field measurements. The method was to experiment on grounding grids comprised of a different number of meshes having the same general geometric configuration. This enabled the authors to establish a correlation for the ground potential rise, step and touch based and the number of meshes, which allowed the authors to investigate how various compression ratios (shown in Figure 5.1) would affect the

overall ground potential rise, step and touch voltages as the number of meshes were increased. The compression ratio of the grounding grid only changes the spacing between the conductors, whereas it does not change the actual number of conductors or their size. This is important as part of the optimization process could change both the number of the conductors and their actual size.

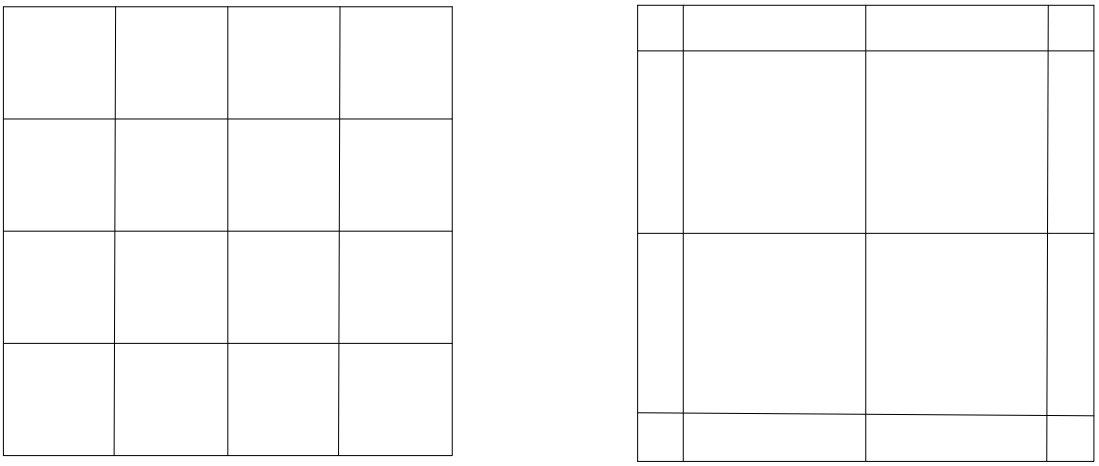

5.1(a) Grounding Grid with No Compression

5.1(b) Grounding Grid with Compression

Figure 5.1 Grounding grid illustrations.

Figure 5.1(a) illustrates a grounding grid with 4 meshes of equal spacing prior to the compression optimization process that these researchers investigated, while Figure 5.1(b) illustrates the grounding grid with 4 meshes of unequal spacing after the compression ratio optimization process from [15, 16]. In their work, they determined that the outer boundaries of the grounding grid had higher step and touch voltages, and, by compressing the grid conductors as shown in Figure 5(b), they were able to reduce the step and touch voltages to safe values.

The next development in the optimization for grounding grid design came from [44, 45], where the authors used the findings from [14 -16] to improve the compression ratio optimization technique and to improve the results. The authors found that the closer the conductors were near the corners, the lower the ground potential rise, and step and touch voltages decreased by approximately 10%. These results were then advanced by [46] with the introduction of a novel optimization technique using genetic algorithms by still using compression ratios as the baseline criteria for the optimization itself. Later, a new approach was developed in [47], where the authors presented a computation of electric fields to develop an optimization technique using a point charge simulation. A novel technique of maximizing the point charge distribution was

used. This technique tried to overcome the equipotential boundary requirement where the charge distribution was optimized through the simulation process. The model worked similarly to the compression ratio optimization method in that the authors found that, at the outer boundary of the grounding grid, it was necessary to increase the field with point charges, but with limited success; however, the method did not provide a cost function based optimization solution.

Up until the work done in [44], researchers had optimized the compression ratio, whereas in [45] optimization was obtained by the use of a set of reflective coefficient curves. These curves were used as the basis of comparison to numerically determine the optimized compression ratio for a specified grounding grid and this was the last attempt at optimization of the grounding grid. This method of optimization was not based on a cost function. Further studies developed the compression ratio optimization process [48-51]; however, these works still did not develop a cost function that is required in a true optimization process which should be based on minimizing actual costs.

This chapter uses the equations presented in previous chapters in the formulation of a cost function that minimizes the cost of the installation of the grounding grid. This research optimized the grounding grid configuration by allowing the size of conductors, number of meshes and number grounding rods to vary through an optimization process which found the minimal cost required to produce a ground grid design that meet the minimum safety requirements at a given electrical station location.

5.2 Mathematical Formulation of the Objective Function

A general optimization model is proposed that consists of several decision variables (having values 0 or 1). The problem can be stated as an objective function representing the fixed costs corresponding to the investment in a grounding grid, subject to the safety criteria established by the IEEE 80-2000[1] at the specific installation site. For the purposes of this research, these values were assumed; however, it should be noted at different sites throughout the world, the installation and materials may vary significantly. For example, the soil characteristics, fault levels, and the available space for the grounding grid itself could vary significantly. The actual parameters used in the objective function are listed in Table 5.1 as shown below.

Table 5.1 Optimization Parameters

Coefficient	**Cost Associated with each parameter**	
rodcost	3 meter ground rod $24 6 meter ground rod $48	
rodinstallcost	installation cost of grounding rod ($/m) 3 m: $48/m 6 m: $78/ m	
rodlen	length of grounding rod (m) 3 meter or 6 meter	
rodnum	number of grounding rods	
xconcost	construction costs per conductor size (AWG) in the x direction ($/m)	
	2/0 4/0 250 350	$85/meter $85/meter $170/meter (manpower/connectors double) $170/meter (manpower/connectors double)
xlengthcost	cost per conductor size (AWG) in the *x* direction ($/m)	
	2/0 4/0 250 350	$8.03/meter $12.70/meter $28.50.meter $39.70/meter
xlength	length of conductors in *x* direction (m)	
xnum	number of conductors in *x* direction (m)	
yconcost	construction costs per conductor size (AWG) in the x direction ($/m)	
	2/0 4/0 250 350	$85/meter $85/meter $170/meter (manpower/connectors double) $170/meter (manpower/connectors double)
ylengthcost	cost per conductor size (AWG) in the *x* direction ($/m)	
	2/0 4/0 250 350	$8.030/meter $12.70/meter $28.50/meter $39.70/meter
ylength	length of conductors in *y* direction (m)	
ynum	number of conductors in *y* direction (m)	

The objective function consists of minimizing the installation costs associated with the grounding grid, as expressed by the following equation:

Minimize

$$[(rodnum * rodlen(m) * rodinstallcost\left(\frac{\$}{m}\right) + rodnum * rodcost(\$)) + (xnum * xlength(m) * \left(xlengthcost\left(\frac{\$}{m}\right) + xconcost\left(\frac{\$}{m}\right)\right) + (ynum * ylength(m) * \left(ylengthcost\left(\frac{\$}{m}\right) + yconcost\left(\frac{\$}{m}\right)\right) \quad (5.1)$$

subject to:

$GPR_{max} \geq GPR_{calculated} \geq .95 * GPR_{max}$

where the cost variables are summarized in Table 5.1

Equation 5.1 represents the cost decision variables with the associated cost coefficients subject to the identified constraint. The number of meshes that formed the grounding grids were one of the search parameters identified in Equation 5.1. The cost function (5.1) for both material and construction are determined independently in the *x* direction and *y* directions. These meshes were allowed to be either a square or rectangular in shape, as shown in Figure 5.2.

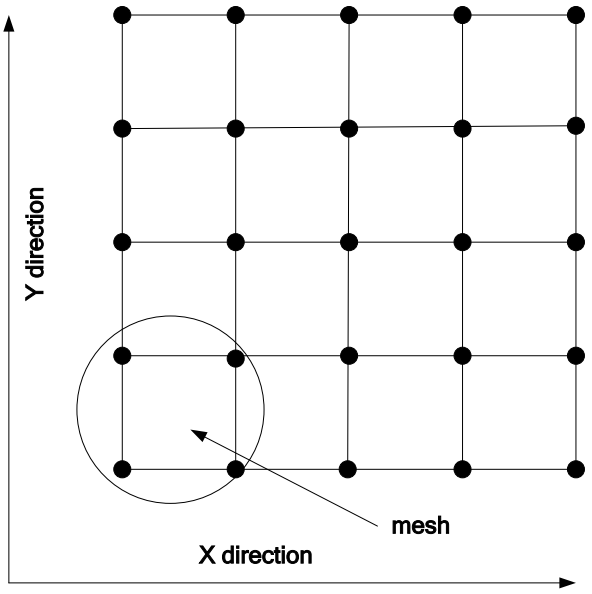

Figure 5.2 Depictions of ground meshes in the X and Y direction.

A MATLAB function was developed that allowed the number of meshes to vary as part of the optimization routine, and, as the search pattern evolved, the grounding grid changed in shape. In the example grounding grid shown in Figure 5.2, there are four meshes in the x direction and four meshes in the *y* direction. These meshes are then combined which will determine the number of conductors in both directions. At each connection point, there are grounding rods which go into the earth, represented by the black dots. Figure 5.3 shows the ground rods from a two dimensional perspective. Each conductor is then represented by three spheres as discussed in Chapter 4 and solved by converting the equations into MATLAB code.

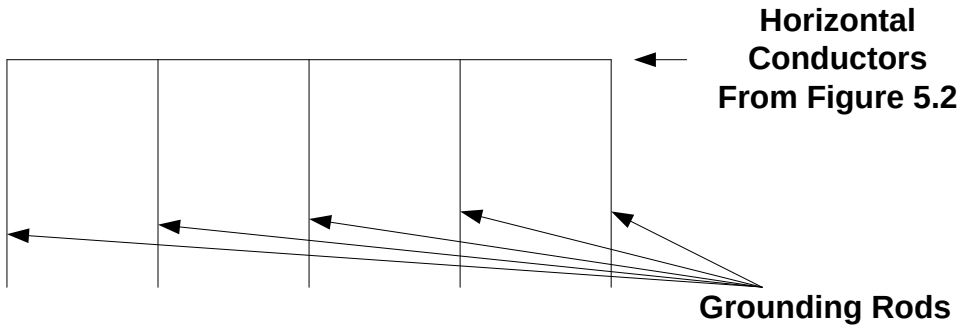

Figure 5.3 Cross sectional view of grounding grid.

The grounding resistance was split into two parameters, the horizontal conductors and the vertical ground rods. In [5], this technique allowed for faster convergence of the calculations of the grounding resistance. Each time the grounding grid is calculated, the constraints outlined in Equation 5.1 ensure that the safety parameters (step and touch voltages) still meets the values from Table 5.2. The actual values for the touch and step voltage constraints were taken from Table 52 (reproduced as Table 5.2) of the Canadian Electrical Safety Code [52], and Section 36 provided the limits of the GPR, which is typically 5000V for most substations, as the Canadian Electrical Safety Code is based on the safety parameters identified in the IEEE80-2000[1]. Therefore, it is necessary to achieve a value of R_g which ensures that the GPR is less than 5000V.

Table 5.2 Exert from the Canadian Electrical Safety Code [52].

Table 52 **Tolerable touch and step voltages** (See Rules 36-304, 36-306, 36-308, 36-310, and 36-312					
Type of ground	Resistivity	Fault duration 0.5 s		Fualt duration 1.0s	
	Ω.m	Step voltage, V	Touch voltage, V	Step voltage, V	Touch voltage, V
Wet Organic soil	10	174	166	123	118
Moist Soil	100	263	188	186	123
Dry Soil	1000	1154	405	816	186
150mm crushed	3000	3143	885	2216	626
stone	10,000	10,065	2569	7116	1816

Notes: Table values are calculated in accordance with IEEE80 [1]

(1) A typical substation installation is designed for 0.5s fault duration, and the entire ground surface inside the fence is covered with 150mm of crushed stone having a resistivity of 3000 Ω.m.

Using the current density in each segment of the grid, the electric potential, V_p, at any point *P* in the soil can be computed by:

$$V_p = \sum_{i=1}^{N} \frac{\mathrm{i}_1}{L_i} \int_{\mathrm{L_i}} \mathrm{G(r, r')dr'} \tag{5.2}$$

where N is the number of segments,

i_1 is the current density of the given segment,

L_i is the length of the given segment, and

$G(r,r')$ is the green function developed in chapter 4.

The touch potential was then determined using Equation 5.3:

$$V_T = GPR - V_P \tag{5.3}$$

where V_T = touch potential

GPR = grid potential rise relative to remote ground

V_P = surface potential at point *P* relative to remote ground

The GPR is solved by multiplying the available fault current by the grounding grid resistance itself [1].

The step potential is obtained by:

$$V_S = Max\ (V_{p2} - V_{p1}) \tag{5.4}$$

where V_s is the step potential and V_{p1} and V_{p2} are the surface potential at two points separated by 1 meter, as outlined in [1]. The values of V_T and V_S depend on the soil resistivity and the density of conductors used in the grid.

5.3 Random Walk Formulation

A random search method typically involves an iterative process in which the search moves successively from the current solution to a randomly-selected new (possibly better) solution in the neighbourhood of that solution. This implies that the neighbourhood structure must be well-connected in a certain precise mathematical sense so that the search may converge for all initial solutions (53). Random search methods have been mainly used for discrete variable optimization problems although there is no particular theoretical reason that prevents applying them to continuous optimization problems. Random search methods are of special appeal for their generality and existence of theoretical convergence proofs (54). The general random search, also summarized by [60], is as follows:

(1) Set an iteration index, $i = 0$. Select an initial solution, θ_i, and perform the simulation to obtain expected value, $X(\theta_i)$.

(2) Select a candidate solution, θ_c, from the neighbourhood of the current solution, $N(\theta_i)$, according to some pre-specified probability distribution and perform the simulation to obtain expected value, $X(\theta_c)$.

(3) If the candidate satisfies the acceptance criterion based on the simulated performance, then, $\theta_{i+1} = \theta_c$; otherwise, $\theta_{i+1} = \theta_i$.

(4) If the termination criterion is satisfied, then terminate the search; otherwise, set $i = i+1$ and go back to Step 2.

Different random search methods found in the literature primarily vary in the choice of the neighbourhood structure, the method of candidate selection, and the acceptance and termination criteria (53). The best known variants of the random search methods are the stochastic ruler algorithms, originally proposed by [54], and those based on the simulated annealing approach. Detailed discussions on random search methods can be found in [54, 55]. The solution of the optimization problem developed in Section 5.2 can be solved. With a Random Walk technique, a minimum value of R_g can be determined while still maintaining the objective function constraints. Random walk Monte Carlo methods (sometimes called Markov

chain and Monte Carlo methods, or MCMC methods) are a class of algorithms to numerically calculate multi-dimensional problems. In these methods, an ensemble of "walkers" moves around randomly. At each point where the walker steps, the integrand value at that point is counted towards the integral. The walker then may make a number of tentative steps around the area, looking for a place with reasonably high contribution to the integral to move into next. Random walk methods are a kind of random simulation or Monte Carlo method. To this end, a brief discussion and selection of the sampling theory used in this thesis will follow.

5.3.1 Sampling Techniques Used in for the Random Walk Methods

Markov chain Monte Carlo methods are those where the direction where a walker is likely to move depends only on where the walker is, and the function value in the area. These methods are easy to implement and analyse, but, unfortunately, it may take a long time for the walker to explore all of the space. The walker may often double back and cover ground already covered. This problem is called "slow mixing." More sophisticated algorithms use some method of preventing the walker from doubling back. For example, in "self avoiding walk," or SAW routines, the walker remembers where it has been before (at least for a few steps), and avoids stepping on those locations again. These algorithms are harder to implement, but may exhibit faster convergence (i.e., fewer steps for an accurate result). Multi-dimensional integrals often arise in Bayesian statistics and computational physics, so random walk Monte Carlo methods are widely used in those fields. The different type of random walk algorithms are summarized below.

5.3.2 Random walk algorithms

In mathematics, rejection sampling is a technique that will generate observations from a distribution with another distribution, known as a proposal density, from which samples can be drawn. Samples are drawn from the proposal density then conditionally rejected to ensure that the samples approximate the target density. This method is simple but does not scale well in high dimensions and in the case of a grounding grid, the random walk does. Adaptive rejection sampling takes a variant of rejection sampling that modifies the proposal density on the fly [60]. The Metropolis-Hastings algorithm generates a random walk using a proposal density and a

method for rejecting proposed moves [55]. Gibbs sampling requires all the conditional distributions of the target distribution to be known in closed form [56, 57]. Gibbs sampling has the advantage that it does not display random walk behavior. However, it can run into problems when variables are strongly correlated. When this happens, a technique called simultaneous over-relaxation can be used [56, 57].

The Hybrid Markov chain Monte Carlo [58] method tries to avoid random walk behaviour by introducing an auxiliary momentum vector and implementing Hamiltonian dynamics where the potential function is the target density. The momentum samples are discarded after sampling. The end result of Hybrid MCMC is that proposals move across the sample space in larger steps and are therefore less correlated and converge to the target distribution more rapidly [58-60]. Slice sampling depends on the principle that one can sample from a distribution by sampling uniformly from the region under the plot of its density function. This method alternates uniform sampling in the vertical direction with uniform sampling from the horizontal "slice" defined by the current vertical position [61]. For the purposes of this research, the Markov Chain Monte Carlo Method (MCMC) from [62] was used as the basis of the optimization process.

5.3.3 Development of the Proposed Method of Optimization

The proposed method of optimization is a general simulation method for sampling from a given distribution and then computing the quantities of interest. The proposed method of optimization takes a sample from a target distribution of the defined parameters to determine the cost of a given grounding grid configuration. Each sample depends on the previous grounding configuration, hence the notion of the Markov chain. A Markov chain then becomes a sequence of random variables, θ_1, θ_2, …, for which the random variable θ^1 depends on all previous θs only through its immediate predecessor θ_{t-1} . Where it moves next is entirely dependent on where it is now; however, it is considered a random walk optimization process. Monte Carlo, as in Monte Carlo integration, is mainly used to approximate an expectation by using the Markov chain samples and it takes the following form:

$$\int_{S}^{\infty} g(\theta)p(\theta)d\theta \cong \frac{1}{n}\sum_{i=1}^{n} g(\theta_t) \tag{5.5}$$

where $g(\cdot)$ is a function of interest, and

θ^t are samples from $p(\theta)$ on its support S.

Equation 5.5 approximates the expected value of $g(\theta)$ of the cost generated by Equation 5.1 for a given grounding grid configuration. This is accomplished by the generation of a sequence of samples from the joint distribution of grounding grid variables outlined in Equation 5.1, and from this sample a grounding grid is formed. When the simulation algorithm was implemented, the value of the cost function converged quite quickly.

The proposed algorithm is summarized as follows [67 & 68]:

(1) Set t=0. Choose a starting point θ_t and this can be an arbitrary point as long as $f(\theta_t|y) > 0$. This is the solution space determined by the number of meshes, number of ground rods, length and width of each mesh determine the initial starting grid.

(2) Generate a new sample, θ_{NEW} , by using a distribution represented by $q(\cdot \mid \theta)$. Calculate the following quantity (Equation 5.6) and determine the cost of the proposed grounding grid. When the cost difference is minimized by Equation 5.1, the optimized grounding grid has been achieved.

$$r = min\left\{\frac{f\{\theta_{new}|y\}}{f\{\theta_t|y\}}, 1\right\} \tag{5.6}$$

(3) Sample u from the uniform distribution U(0,1) .

(4) Set $\theta_{t-1} = \theta_{new}$ if u< r; otherwise set $\theta_{t-1} = \theta_t$.

(5) Set t=t+1. If $t < T$, the maximum number of desired samples, return to step 2. Otherwise, stop.

The number of iteration keeps increasing regardless of whether a proposed sample is accepted. Figure 5.5 shows how the mathematics was used in the determination of the grid itself. The criteria used to determine when to stop the optimization process was when the solution was within 5% of the desired $R_{g,}$ as shown in Figure 5.4. Step and touch voltages were then calculated to ensure that the solution found satisfied the constraints listed in Table 5.2; if not, the solution was rejected and optimization continued.

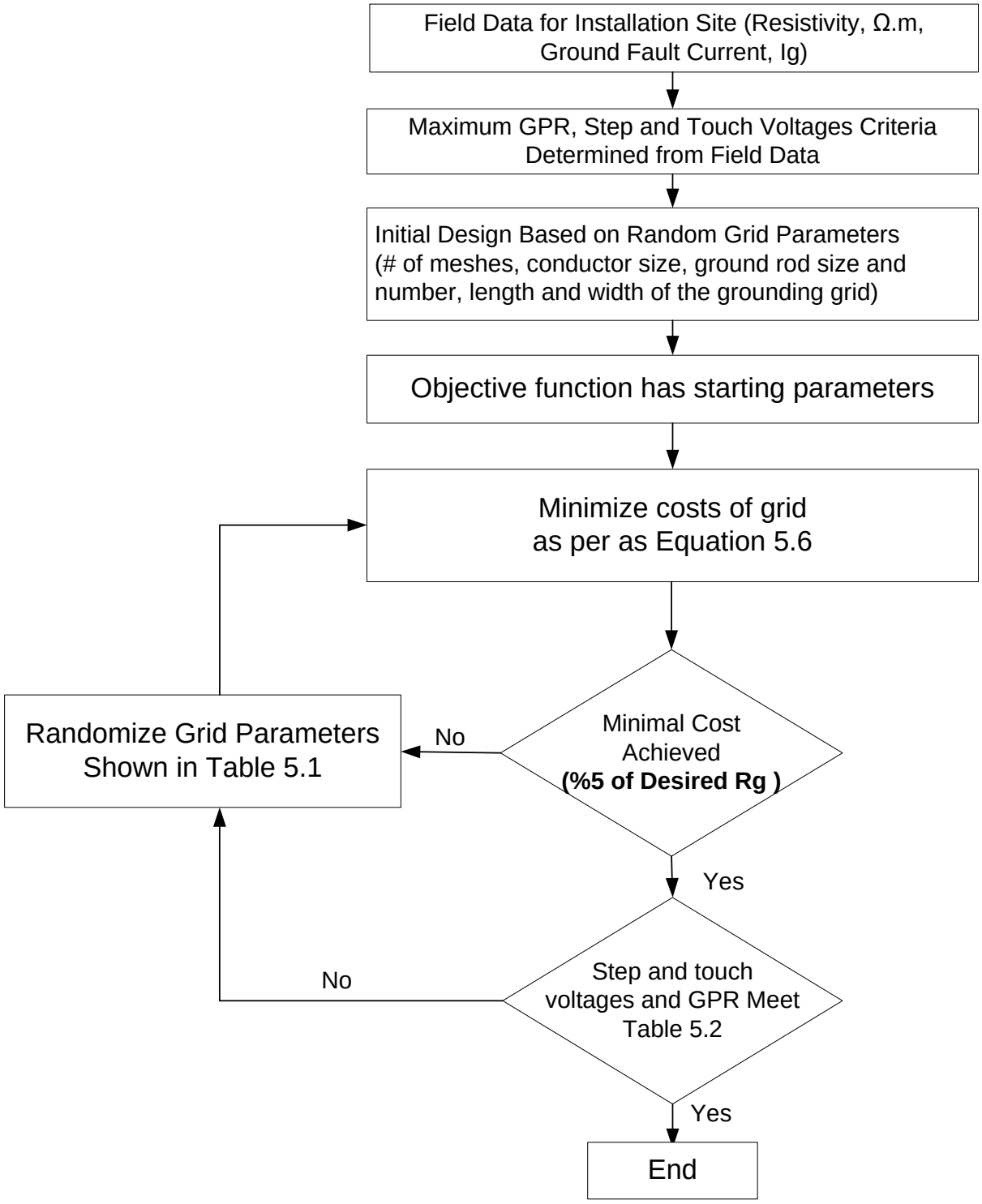

.

Figure 5.4 Methodology of proposed outline to find the optimized grounding grid.

MATLAB functions were generated to randomly select the length of the ground rods as either 3 or 6 meters, and the conductor sizes were either 2/0, 4/0, 250 MCM or 350 MCM based on field experience in grounding systems, as the IEEE and typical electrical codes call for a 2/0 grounding conductor as the minimum size. For the number of meshes, the minimum values were randomly selected between 1 and the maximum value was 100. In the case of the length of *lx* and *ly*, the minimum value was 1 meter and the maximum value was 200 meters, based on field experience of typical high voltage grids. In all test cases, these values proved to be acceptable limitations. However, in the actual software a simple routine can adjust any and all parameters until convergence of the cost function is achieved.

5.4 Case Studies for Optimization Results for Various Ground Systems

To demonstrate the capabilities of the proposed method, existing grids at three high voltage installations from Ontario, Canada were obtained. The soil model optimization from Chapter 3, the proposed Simpson Rule from Chapter 4, and lastly the proposed optimization process discussed earlier were used.

The first case study is an industrial steel plant located in Kingston, Ontario. The starting grounding grid dimensions were side length of 22 meters, with 8 meshes per side and having 12 grounding rods. Figure 5.5 shows the pre-optimized grounding grid that was used as the starting sequence for the optimization process discussed earlier.

After 98 iterations, optimization determined the optimized configuration. The side length increased to 24 meters, while the number of meshes decreased to 4 per side and the grounding rods were reduced to 4. The overall costs were reduced by approximately 50%. SKM grounding software was used to compare the pre-optimized and optimized grounding grid GPR, touch and step voltages to those determined by the software developed for this thesis to verify that the results obtained were realistic and proven correct using commercial software. Table 5.5 shows a summary of the pre-optimized and optimized values with the total costs for both scenarios.

Table 5.3 Case 1: summary of pre-optimized and optimized results

Coefficient	**Pre-optimized Values**	**Optimized Values**
rodcost	$24/grounding rod	$24/grounding rod
rodinstallcost	$48/m	$48/m
rodlen	3-m	3-m
rodnum	12	4
xconcost	$85/meter 4/0 conductor	$85/meter 4/0 conductor
xlengthcost	$12.70/meter 4/0 conductor	$12.70/meter 4/0 conductor
xlength	24 meters	22 meters
xnum	9 conductors	5 conductors
yconcost	$85/meter 4/0 conductor	$85/meter 4/0 conductor
ylengthcost	$12.70/meter 4/0 conductor	$12.70/meter 4/0 conductor
ylength	24 meters	24 meters
ynum	9 conductors	5 conductors
	$44,222.40	$22,166.00

Note: The costs used were provided by the engineering firm that performed the grounding analysis at the time of installation. These numbers may vary with the cost of labor and copper at a given time and in a given region. The cost of backfilling and crushed stoned is a fix price based on the area of the grounding grid itself. Since these parameters are not part of the determination of R_g, they were not included in the optimization process. The area pre-optimization verses the optimized area was negligible in the three different case studies. This value can be added after the optimization process if there are significant changes in the grounding grid area itself.

The optimized grid is shown in Figure 5.5. Note that this figure and the remaining figures in this chapter were produced using the commercial software, SKM, to show that the results are valid and appropriate.

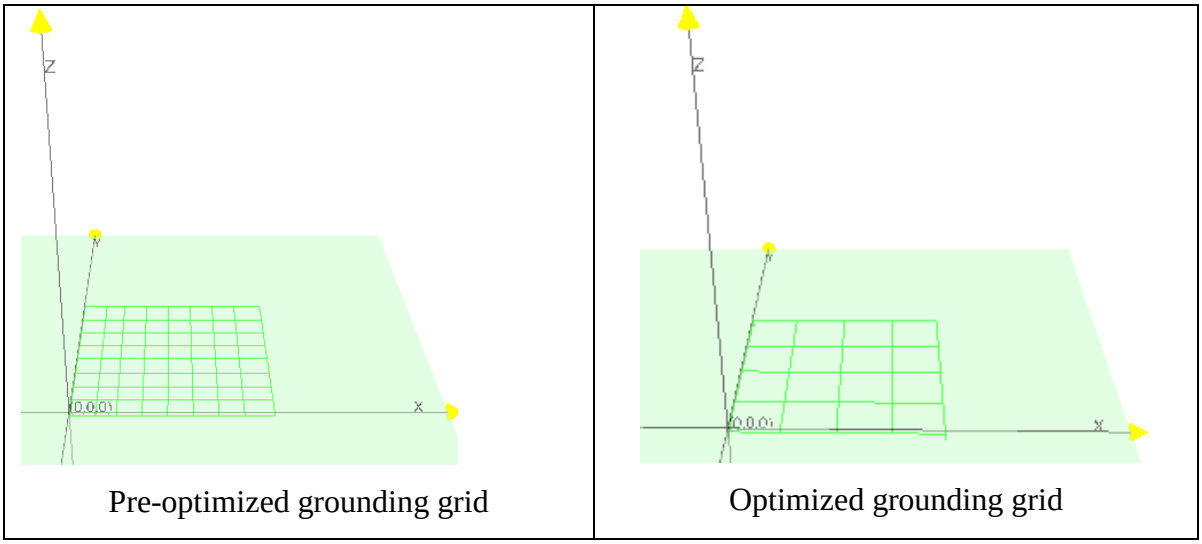

Pre-optimized grounding grid | Optimized grounding grid

Figure 5.5 Existing (pre-optimized) and optimized grounding grids.

Figure 5.6 shows the GPR values of both the pre-optimized and optimized grounding grid. Note that the values are quite similar, and well below the maximum permitted GPR.

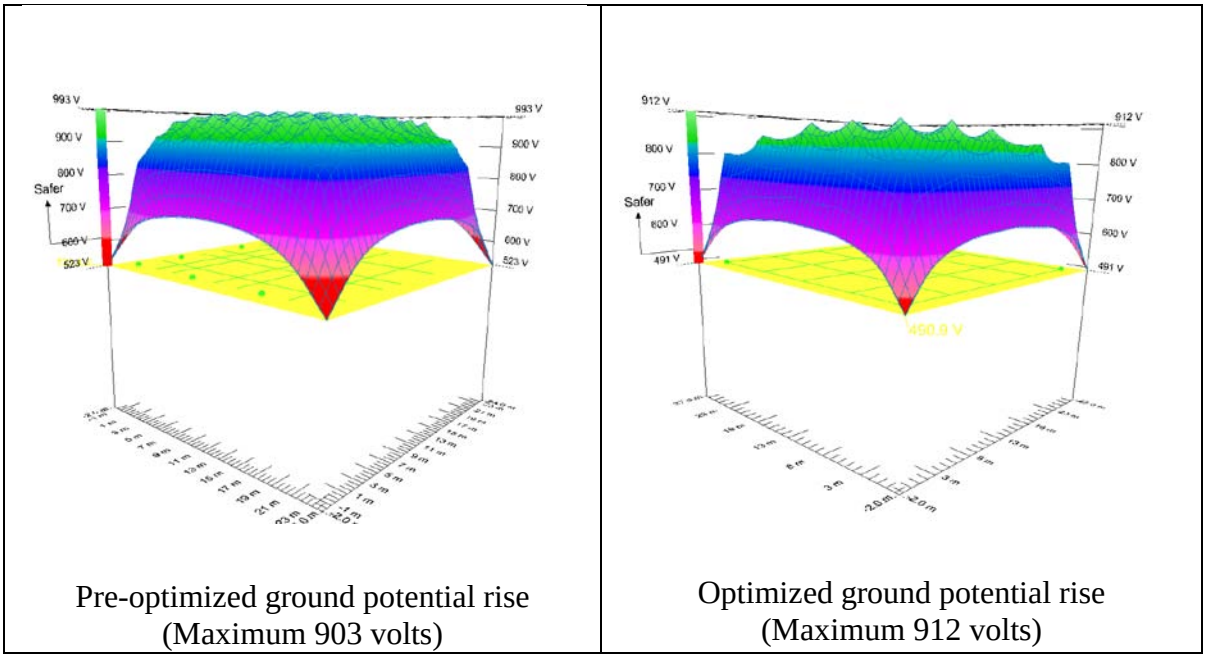

Pre-optimized ground potential rise (Maximum 903 volts) | Optimized ground potential rise (Maximum 912 volts)

Figure 5.6 Existing (pre-optimized) and optimized ground potential rise.

Figure 5.7 shows the touch voltage values of both the pre-optimized and optimized grounding grid. In this case, the touch voltages were actually reduced.

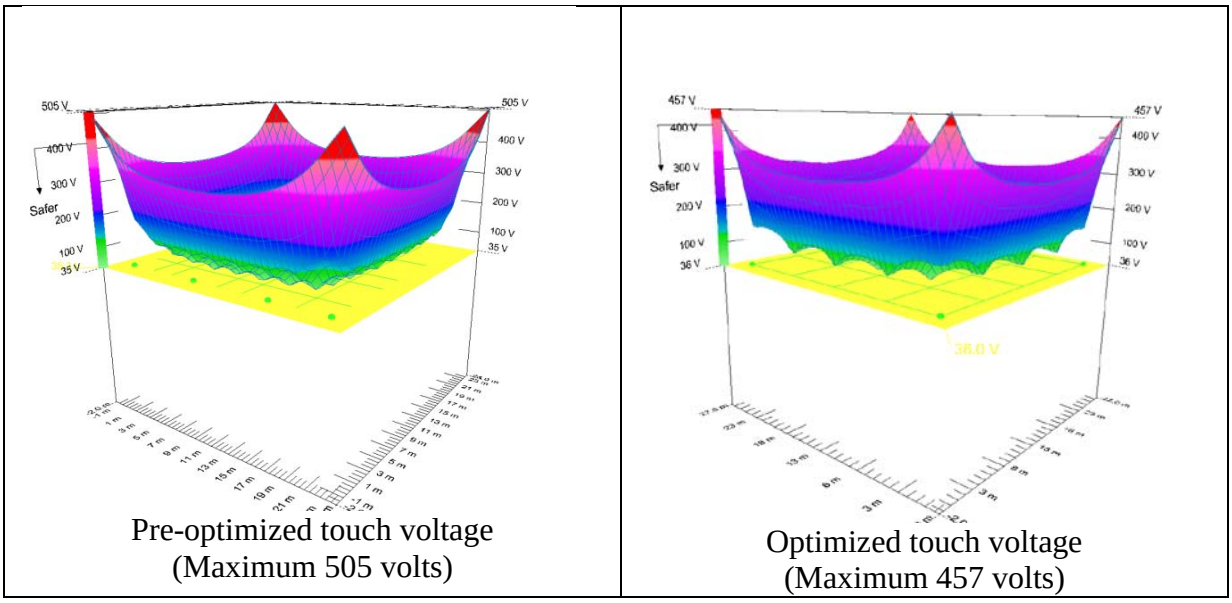

Pre-optimized touch voltage
(Maximum 505 volts)

Optimized touch voltage
(Maximum 457 volts)

Figure 5.7 Existing (pre-optimized) and optimization touch voltage.

Figure 5.8 shows the pre-optimized and optimized step voltages, and here there were no significant changes in values. In the commercial software, R_g was found to be 0.95 Ω (pre-optimized) and 1.03 Ω (optimized) compared to the software developed for this thesis of 0.98 Ω and 0.97 Ω, respectively. These values are comparable and demonstrate the accuracy of the software.

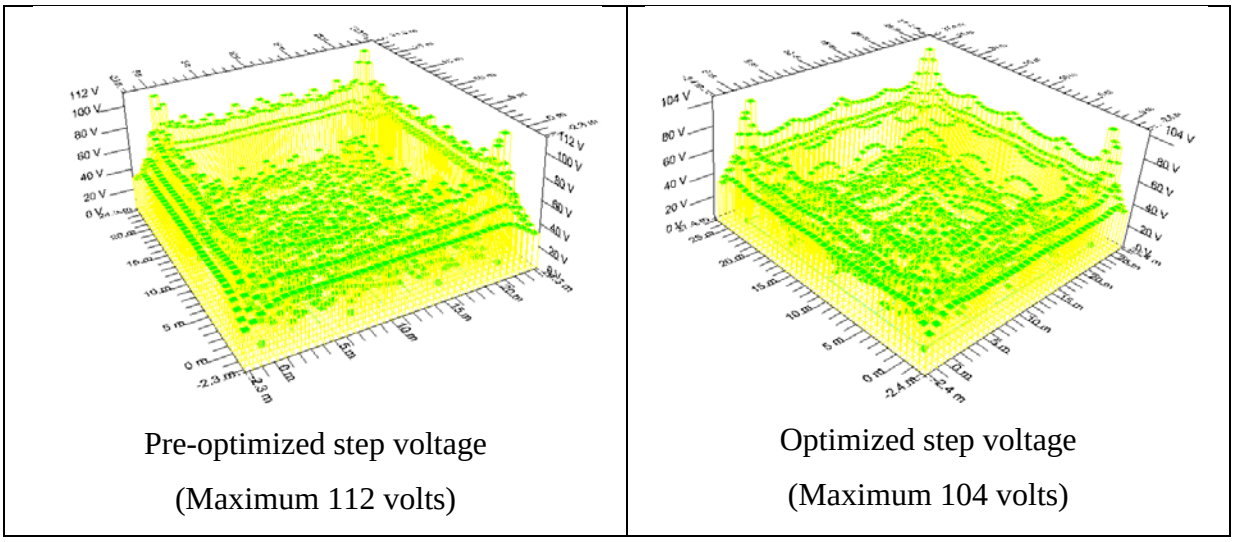

Figure 5.8 Existing (pre-optimized) and optimized step voltage.

The next case study was a commercial installation in Brampton, Ontario. In this example, the soil model required was that of a two layer structure, making the calculations more complicated. The starting grounding grid dimensions were side length of 40 meters, with 17 meshes per side and having 12 grounding rods. After 498 iterations, the optimized configuration was found, which increased the side length to 44 meters, reduced the number of meshes to 5 per side, and the number of grounding rods to four. The overall costs in this case study were reduced 64%. To verify the findings of the program, SKM grounding software was used to compare the pre-optimized and optimized grounding grid GPR, touch and step voltages were determined by the software developed for this thesis. It was found that the optimized grounding grid did not affect the safety requirements for GPR, and the touch and step voltages as demonstrated in subsequent figures for this case study. Figure 5.9 shows the pre-optimized grounding that was used as the starting sequence for the optimization process and the final grid design.

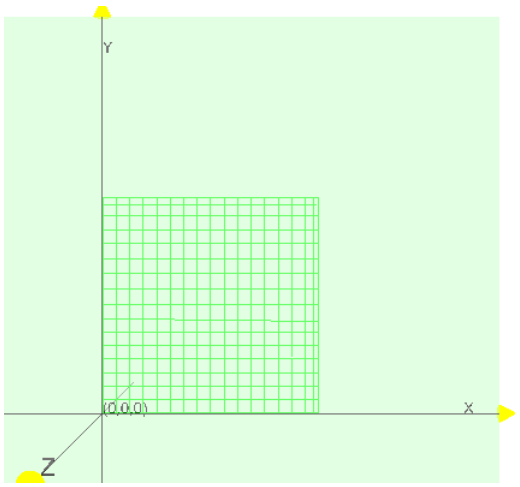

Pre-optimized grounding grid

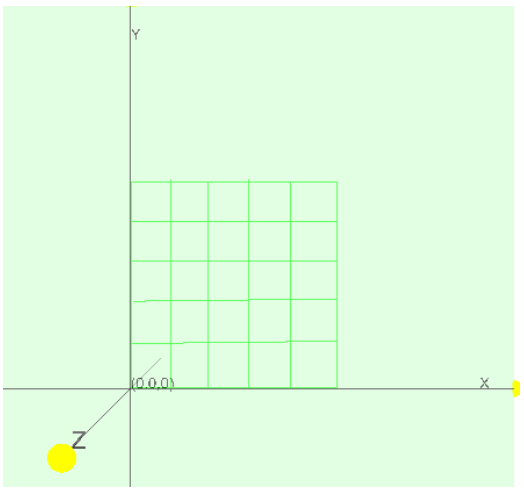

Optimized grounding grid

Figure 5.9 Existing (pre-optimization) optimized grounding grids.

Table 5.4 Case 2: Summary of pre-optimized and optimized Results

Coefficient	**Pre-optimized Values**	**Optimized Values**
rodcost	$24/grounding rod	$24/grounding rod
rodinstallcost	$48/m	$48/m
rodlen	3-m	3-m
rodnum	12	6
xconcost	$85/meter 4/0 conductor	$85/meter 4/0 conductor
xlengthcost	$12.70/meter 4/0 conductor	$12.70/meter 4/0 conductor
xlength	40 meters	44 meters
xnum	18 conductors	6 conductors
yconcost	$85/meter 4/0 conductor	$85/meter 4/0 conductor
ylengthcost	$12.70/meter 4/0 conductor	$12.70/meter 4/0 conductor
ylength	40 meters	44 meters
ynum	18 conductors	6 conductors
	$142,704.00	$52593.60

Note: The costs used were provided by the engineering firm that performed the grounding analysis at the time of installation. These numbers may vary with the cost of labor and copper at a given time and in a given region. The cost of backfilling and crushed stoned is a fix price based on the area of the grounding grid itself. Since these parameters are not part of the determination of R_g, they were not included in the optimization process. The area pre-optimization verses the optimized area was negligible in the three different case studies. This value can be added after the optimization process if there are significant changes in the grounding grid area itself.

Figure 5.10 shows the GPR values of both the pre-optimized and optimized grounding grid. Note that the values are quite similar, and well below the maximum permitted GPR.

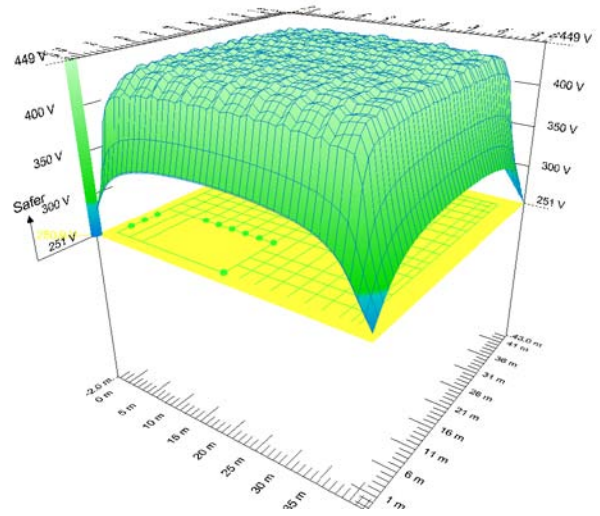

Pre-optimized ground potential rise
(Maximum 449 volts)

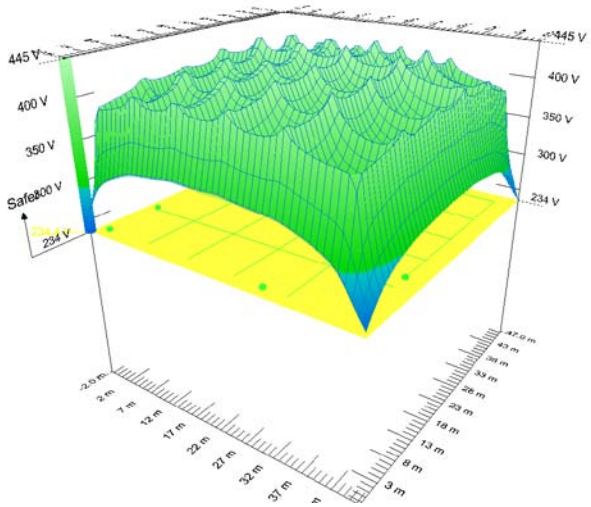

Optimized ground potential rise
(Maximum 445 volts)

Figure 5.10 Existing (pre-optimized) and optimized ground potential rise.

Figure 5.11 shows the touch voltages values of both the pre-optimized and optimized grounding grid. These values are comparable and demonstrate the accuracy of the software.

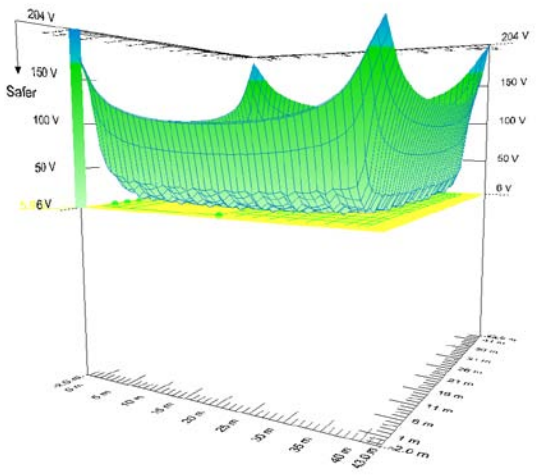

Pre-optimized touch voltage

(Maximum 204 volts)

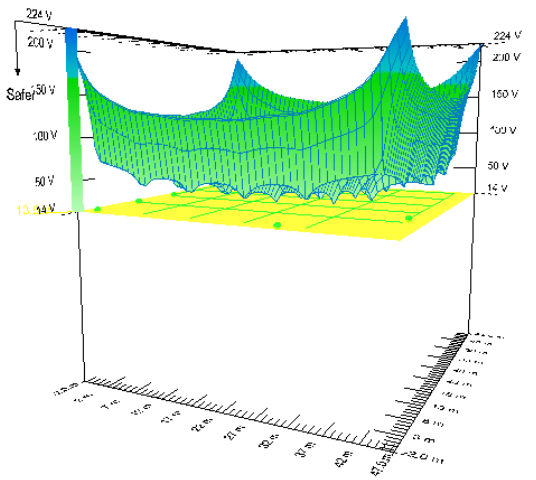

Optimized touch voltage

(Maximum 224 volts)

Figure 5.11 Existing (pre-optimized) and optimized touch voltage.

Figure 5.12 shows the step voltages values of both the pre-optimized and optimized grounding grid. Note that the values are quite similar. In the commercial software, Rg was found to be 4.55 Ω (pre-optimized) and 4.59 Ω (optimized) compared to the values found by the software developed for this thesis of 4.51 Ω and 4.61 Ω, respectively. These values are comparable and demonstrate the accuracy of the software.

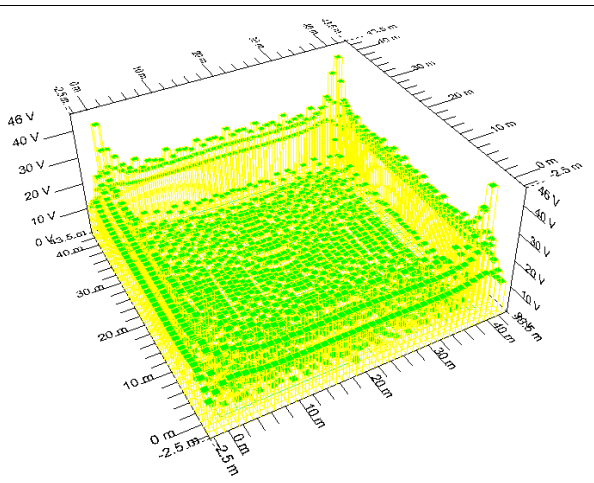

Pre-optimized step voltage

(Maximum 46 volts)

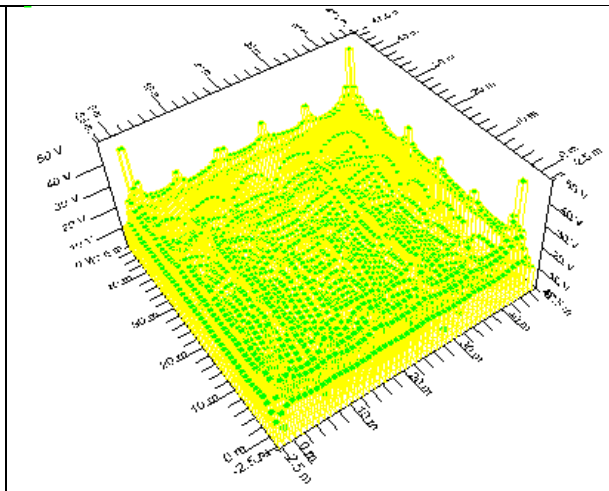

Optimized step voltage

(Maximum 50 volts)

Figure 5.12 Existing (pre-optimized) and optimized step voltage.

The last case study was taken from Sudbury, Ontario, where the soil conditions made grounding design very difficult, as the soil structure was complex in that the lower soil layer actually had a lower resistivity. After 326 iterations, an optimum configuration was found. The overall costs in this case study were reduced 83%. SKM grounding software was used to compare the pre-optimized and optimized grounding grid GPR, and the touch and step voltages determined by the software developed for this thesis.

Figure 5.13 provides the starting grounding grid dimensions side length of 50 meters, with 18 meshes per side and 10 grounding rods. The optimized grid is also shown, having a side length of 46 meters, with 2 meshes per side and 6 grounding rods.

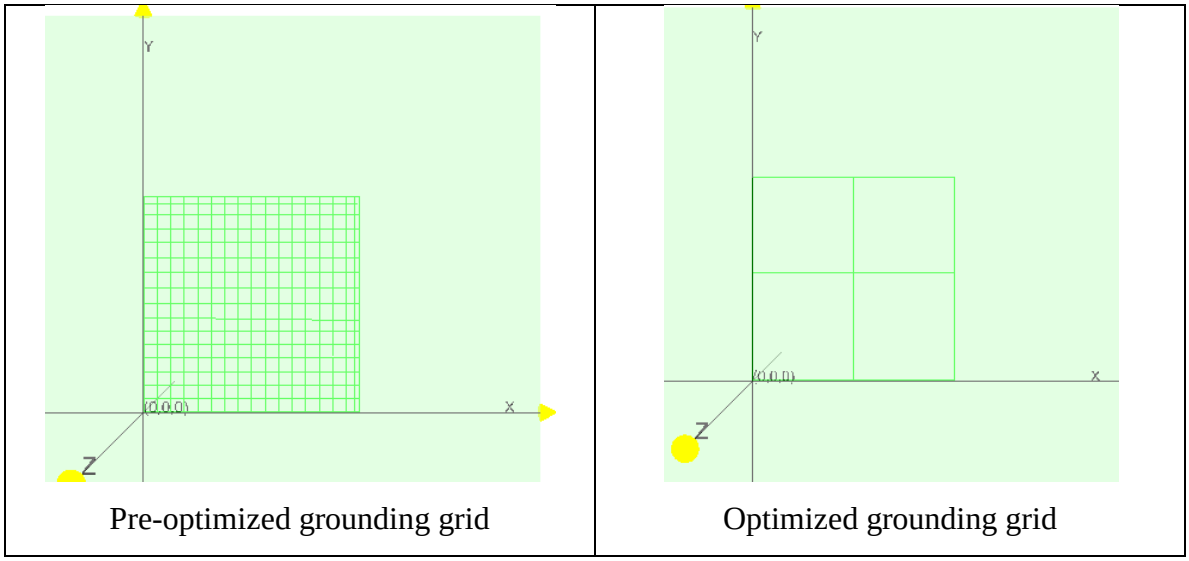

Pre-optimized grounding grid | Optimized grounding grid

Figure 5.13 Existing (pre-optimized) and optimized grounding grids.

Table 5.5 Case 3: Summary of Pre-optimized and Optimized Results

Coefficient	**Pre-optimized Values**	**Optimized Values**
rodcost	$24/grounding rod	$24/grounding rod
rodinstallcost	$48/m	$48/m
rodlen	3-m	3-m
rodnum	10	6
xconcost	$85/meter 4/0 conductor	$85/meter 250MCM conductor
xlengthcost	$12.70/meter 4/0 conductor	$28.50/meter 250MCM conductor
xlength	50 meters	46 meters
xnum	19 conductors	3 conductors
yconcost	$85/meter 4/0 conductor	$85/meter 250 MCM conductor
ylengthcost	$12.70/meter 4/0 conductor	$28.50/meter 250MCM conductor
ylength	50 meters	46 meters
ynum	19 conductors	3 conductors
Total Cost	$187,310.00	$32,334.00

Note: The costs used were provided by the engineering firm that performed the grounding analysis at the time of installation. These numbers may vary with the cost of labor and copper at a given time and in a given region. The cost of backfilling and crushed stoned is a fix price based on the area of the grounding grid itself. Since these parameters are not part of the determination of R_g, they were not included in the optimization process. The area pre-optimization verses the optimized area was negligible in the three different case studies. This value can be added after the optimization process if there are significant changes in the grounding grid area itself.

Figure 5.14 shows the GPR values of both the pre-optimized and optimized grounding grid. Note that the values are quite similar, and well below the maximum permitted GPR.

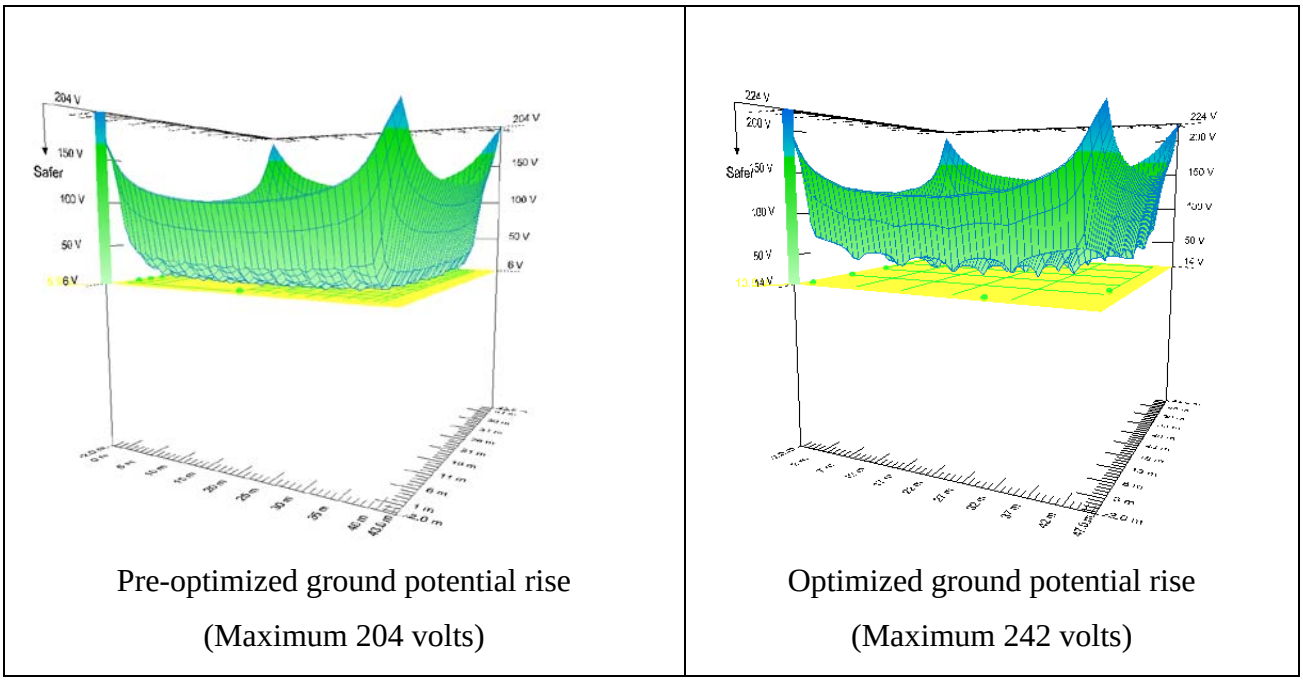

Pre-optimized ground potential rise
(Maximum 204 volts)

Optimized ground potential rise
(Maximum 242 volts)

Figure 5.14 Existing (pre-optimized) and optimization ground potential rise.

Figure 5.15 shows the touch voltages values of both the pre-optimized and optimized grounding grid. Figures 5.15, 5.16 and 5.17 shows the GPR, and the touch and step voltage, respectively, for the existing and optimized grids. In each case, the values are comparable. Figure 5.15 shows the touch voltages values of both the pre-optimized and optimized grounding grid. These values are comparable and demonstrate the accuracy of the software.

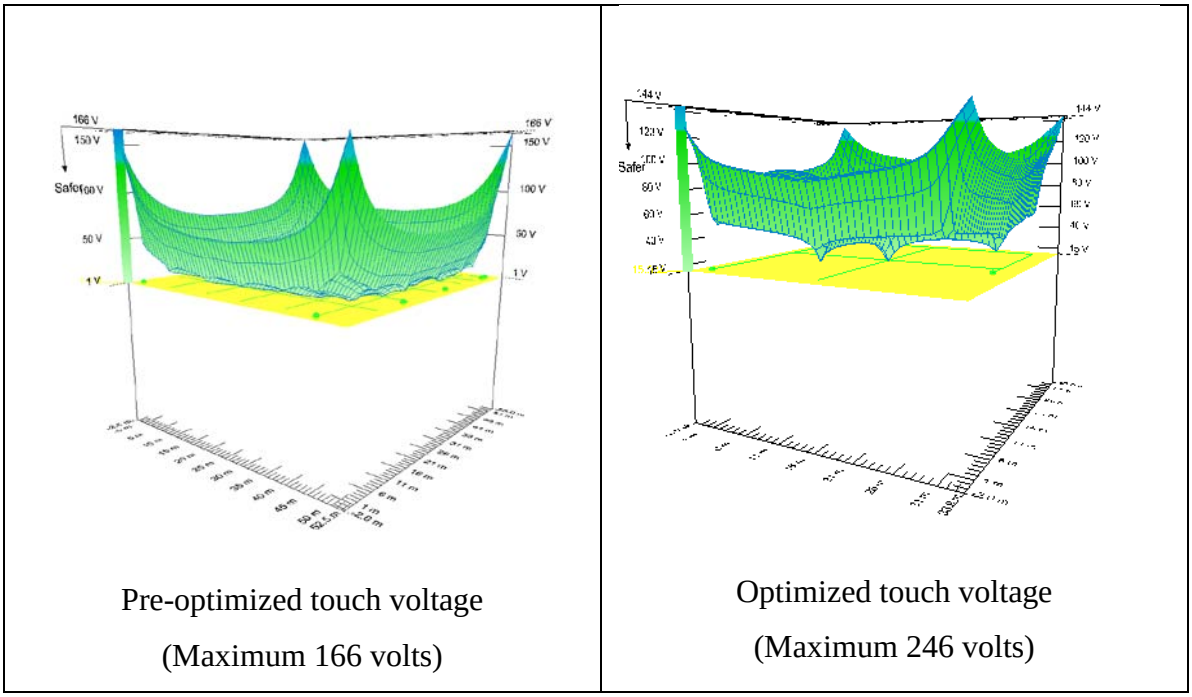

Pre-optimized touch voltage

(Maximum 166 volts)

Optimized touch voltage

(Maximum 246 volts)

Figure 5.15 Existing (pre-optimized) and optimization touch voltage.

Figure 5.16 shows the step voltages values of both the pre-optimized and optimized grounding grid. These values are comparable and demonstrate the accuracy of the software.

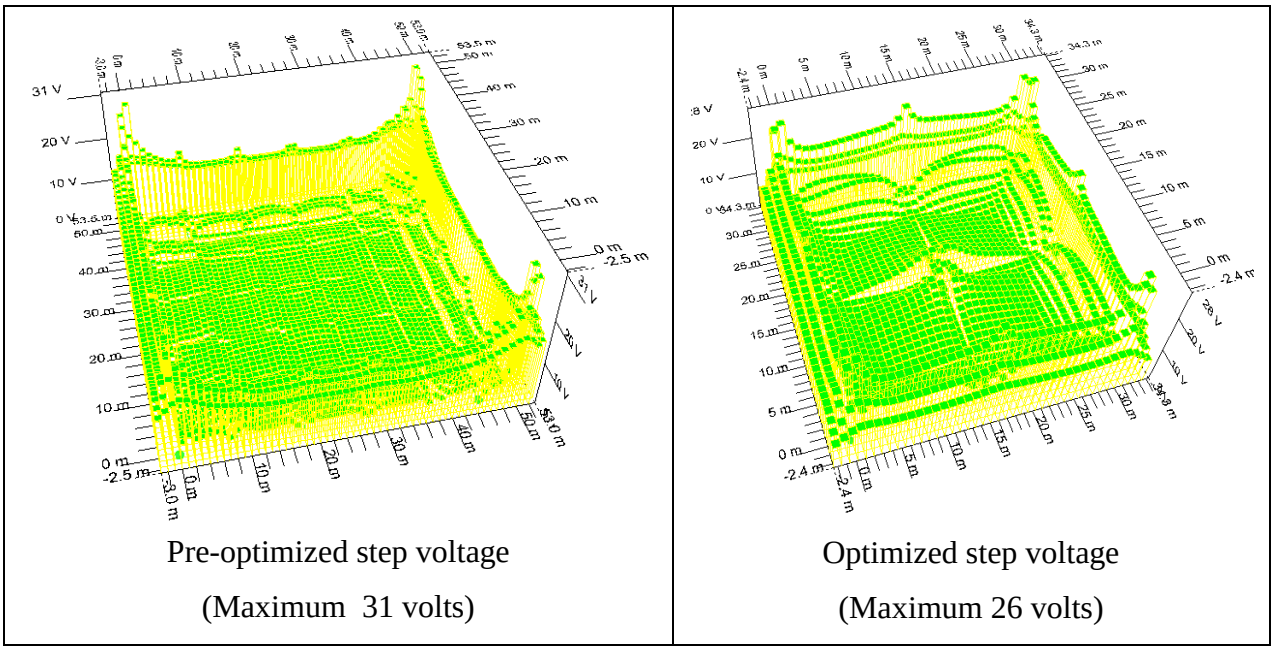

Pre-optimized step voltage

(Maximum 31 volts)

Optimized step voltage

(Maximum 26 volts)

Figure 5.16 Existing (pre-optimized) and optimization step voltage.

Using the commercial software, Rg was found to be 0.96 Ω (pre-optimized) and 1.04 Ω (optimized) compared to values found by the software developed for this thesis of 0.98 Ω and 0.99 Ω, respectively. These values are comparable and demonstrate the accuracy of the software.

5.5 Summary of Proposed Optimization Method

The technique discussed and developed in Chapter 4 allows grounding grid resistance to be quickly determined, further allowing a multitude of grounding grid designs to be assessed and discarded as better solutions are found for a particular installation. This chapter has clearly demonstrated the effectiveness of the technique, and showed cost savings between 40% and 75% could have been achieved had the technique been used in three real life examples. Existing commercial software (SKM) also verified that the method is valid, as the grid resistances calculated by SKM were nearly identical to those calculated by the software developed for this thesis. SKM also proved that the safety parameters of GPR, step and touch voltages were not significantly affected. The proposed technique has the potential to save industry millions of dollars in grounding grid design and installation costs. The examples given within this thesis were implemented successfully in the Province of Ontario, Canada.

Chapter 6 Conclusions and Future Work

6.0 Conclusions

The statement of problem of this research, to improve upon ground grid design, minimizes the total cost of the material and installation costs of the grounding grid, and the objectives, contributions and outline of the dissertation as outlined in Chapter 1.

In this dissertation, previous methods for soil model were reviewed and limitations inherent in them were outlined in Chapter 2. In Chapter 3, a simple analytical formula of the Sunde's curves was derived for the determination of the soil model used in grounding system design. In Chapter 4, a set of matrix equations that were solved numerically through matrix inversion through the use of a novel analysis technique utilizing Simpson's rule of integration was introduced. Chapter 5 then used the soil model and analysis technique to optimize the grounding grid design itself.

The following conclusions can be drawn from this research:

(1) The proposed soil model analysis has proven to be accurate and more reliable than current modeling techniques. The unique feature of this part of the dissertation is this was the first time that the soil model was found directly from field measurements while at the same optimizing the results. This research provided a discussion of the parameters that affect grounding grid design, the importance of a good soil model, and a survey of existing techniques used to finds those models. One of the commonly used methods is the graphical Sunde which is based on complex images. Researchers have advanced some of the original technique developed by the Sunde curves for comparison during calculations; however, there has been little effort in determining the soil model directly from the field measurements themselves. The research provided a new method to determine the soil model parameters directly from field measurements, based on equations that replace the Sunde curves and then use techniques involving multiple complex images.

With the simple and rigorous expressions of the Sunde's curves, the extraction of the soil model of the two-layer soil is now very simple and automatic when run as a computer program. As shown in Tables 3.3 and 3.4, the accuracy is high. Finally, the computation time required for other methods ([13], [17] and [19]), as well as the asymptotic approximation of Chapter 3, are all very small. The main advantage of the

asymptotic approximation presented in this research lies in its analytical simplicity, that is, as compared to other software in which the complexity of the multiple image and numerical approach, in direct space or spectral space as discussed in the introduction. This simplicity gives clear insights and indicates that it should be possible in the future to modify the one asymptote in the intermediate transition region to extend the asymptote approach to three layer soil, or even to multilayer soil; the computing routine should remain fast.

(2) The Simpson's rule of integration has proven to simplify the numerical techniques used to date. Good agreement was found between this proposal and the other data available in research while reducing the computational burden inherent within this type of analysis. This research provided the specific numerical formulations required to determine the grounding grid resistance. The authors in [26] introduced spheres to improve the boundary conditions; however, the short coming of their approach was that it required designer intervention to add spheres at the end. This research provided a new method for a more systematic approach for sphere placement, and this method also reduced errors in calculating the resistance.

(3) The optimization of the grounding grid has reduced costs for the grounding grid without jeopardizing any of the safety parameters required and discussed in this thesis. This part of the dissertation took advantage of the advancements in Chapters 3 and 4 in order to offer a novel optimization process whereby a grounding grid design is optimized based on costs. The results were compared with commercial software with excellent agreement.

(4) The technique discussed and developed in this thesis allowed the grounding grid resistance to be quickly determined, allowing a multitude of grounding grid designs to be assessed and discarded as better solutions were found for a particular installation. This research has clearly demonstrated the effectiveness of the technique, and showed cost savings between 40% and 75% could have been achieved had the technique been used in three real life examples. Existing commercial software (SKM) also verified that the method is valid, as the grid resistances calculated by SKM were nearly identical to those calculated by the software developed for this thesis. SKM also proved that the safety parameters of GPR, step and touch voltages were not significantly affected. The

proposed technique has the potential to save industry millions of dollars in grounding grid design and installation costs.

6.1 Recommendations for Future Work

The following suggestions are offered for future work:

(1) some areas of the world would necessitate soil models that are not uniform or two layer, but rather multiple layers, and the method developed here should be extended to such cases;

(2) extend the methods developed here to grids of arbitrary shapes; and,

(3) extend the methods developed here to account for nearby structures, buried cables and pipes, etc.

References

[1] *IEEE Guide for Safety in AC Substation Grounding*, The Institute of Electrical and Electronic Engineers, Inc., New York, 2000.

[2] *IEEE Guide for Measuring Earth Resistivity, Ground Impedance, and Earth Surface Potentials of A Ground System*, The Institute of Electrical and Electronic Engineers, Inc., New York, 1983.

[3] J.S. Schwarz, "Analytical expressions for resistance of grounding systems," *AIEE Transactions*, vol. 73, pp. 1011-1016, Aug. 1954.

[4] M.M.A. Salama, M. Elsherbiny, Y.L. Chow, "Calculation and interpretation of resistance of grounding grid in two-layer soil with synthetic asymptotic approach," *Electric Power System Research Journal*, vol. 35, no. 3, pp. 157-165, Oct. 1995.

[5] Y.L. Chow, and M.M.A. Salama, "A simplified method for calculating the substation grounding grid resistance," *IEEE Trans. on Power Delivery*, vol. 9, pp. 736-742, Feb. 1994.

[6] B. Nekhoul, P. Labie, F.X. Zgainski, and G. Meunier, "Calculating the impedance of a grounding system," *IEEE Trans. on Magnetics*, vol. 32, pp. 1509-1512, May 1996.

[7] M.M. Elsherbiny, Y.L. Chow, M.M.A. Salama, "A fast and accurate analysis of grounding resistance of a driven rodbed in two-layer soil," *IEEE Trans. on Power Delivery*, vol. 11, pp. 808-814, Apr. 1996.

[8] M.M.A. Salama, M.M. Elsherbiny, Y.L. Chow, "A formula for resistance for substation grounding grid system in two-layer soil," *IEEE Trans. on Power Delivery*, vol. 10, pp. 736-742 Jul. 1996.

[9] E.D. Sunde, *Earth conduction effects in transmission systems*. New York: McMillan, 1968.

[10] R.J. Heppe, "Computation of potential at surface above an energized grid or other electrode, allowing for non-uniform current distribution," *IEEE Trans. on Power Apparatus and Systems*, vol. PAS-98, pp. 1978-1989, Nov./Dec. 1979.

[11] L.S. Palmer, "Examples of geotechnical surveys," *Proceedings of the IEE*, vol. 2 Paper 106, Jun. 1959.

[12] Chen Jing and Gao Yougang, "Resistive coupling of crossing buried conductors," *Communication Technology Proceedings*, vol.1, pp. 22-24, Oct 1998.

[13] F. Dawalibi and C. J. Blattner, “Earth Resistivity Measurement Interpretation Technique,” *IEEE Trans. on Power Apparatus and Systems,* vol. PAS-103, no. 2, pp. 374 – 382, Feb. 1984.

[14] F.P Dawalibi, and D. Mukhedkar, “ Optimum design of substation grounding in two-layer earth model—Part I analytical study,” *IEEE Trans. in Power Systems Applications,* vol. PAS-94, pp. 252-261, Mar./Apr.1975.

[15] F. Dawalibi, and D. Mukhedkar, “Optimum design of substation grounding in two-layer earth model- Part II analytical study,” *IEEE Trans. in Power Systems Applications,* vol. 94, pp. 262-266, Mar./Apr. 1975.

[16] F. Dawalibi and D. Mukhedkar, “Optimum design of substation grounding in two-layer earth model- Part.III analytical study,” *IEEE Trans. in Power Systems Applications,* vol. 94, pp. 267-272, Mar./Apr. 1975.

[17] Hans. R. Seedher and J. K. Arora, “Estimation of two layer soil parameters using finite Wenner resistivity expressions,” *IEEE Trans. on Power Delivery,* vol. 7, no. 3, pp. 1213 - 1217, Oct. 1993.

[18] J. L. del Alamo, “A comparison among eight different techniques to achieve an optimum estimation of electrical grounding parameters in two-layered earth,” *IEEE Trans. on Power Delivery,* vol. 8, no. 4, pp. 1890 – 1899, Oct. 1993.

[19] Ioannis Gonos and Ioannis Stathopulos, “Estimation of multilayer soil parameters using genetic algorithms,” *IEEE Trans. on Power Delivery,* vol. 20, no. 1, pp. 100 - 106, Jan. 2005.

[20] Y.L. Chow and W.C. Tang, “Development of CAD formulas of integrated circuit components,” *J. of EM Waves and Appl.*, vol. 15, no.8, pp. 1097-1119, Aug. 2001.

[21] Wanchun Tang, Tingshan Pan, Xiaoxiang He, and Y. Leonard Chow, “CAD formulas of the capacitance to ground of square spiral inductors with one or two layer substrates by synthetic asymptote,” *Microwave and Optical Technology Letters,* vol. 48, no. 5, pp. 972-977, May 2006.

[22] M. Abramowitz and I. A. Stegun (Ed.), *Handbook of Mathematical Functions*, National Bureau of Standards, Applied Mathematics, Series 55. Jun. 1964, pp. 378.

[23] R.F.Harrington, *Field Computations by Moment Methods*. New York: McMillan, 1968.

[24] Y.L. Chow, M.M.A. Salama, G. Djogo, "The source resistances of the touch, transferred and step voltages of a grounding system," *IEE Proceedings on Generation, Transmission and Distribution,* vol. 46, pp. 107-114, Mar. 1999.

[25] Y.L. Chow, M.M. ElSherbiny, and M. M. Salama, "Efficient computation of the rodbed grounding resistance in a homogenous earth by Galerkin's method," *IEE Proceedings, Generation, Transmission and Distribution,* vol. 142, pp. 653-660, Nov. 1995.

[26] Y.L. Chow, M.M. ElSherbiny, and M. M. Salama, "Surface voltages and resistance of grounding systems of grid and rods in two-layer earth by the rapid Galerkin's moment method," *IEEE Trans. on Power Delivery*, vol. 17, pp. 45-45, Jan. 1997.

[27] Y.L. Chow, M.M. ElSherbiny, M.M.A Salama, and A.Y.Chikhani, Simulated test method for earth resistance measurements in single layer soil," *Applied Modeling, Simulation and Optimization Conference*, Cancun, Mexico, 1996, pp. 89-90.

[28] H.B. Dwight, "Calculation of Resistance to Ground," *American Institute of Electrical Engineering*, vol. 55, pp. 1319 - 1328, Dec 1936.

[29] P. G. Laurent, "Les Bases Generales de la Technique des Mises a la Terre dans les Installations Electriques," *Bulletin de la Societe Francaise des Electriciens,* vol. 1, ser. 7, pp. 368–402, Jul. 1951.

[30] J. Nieman, "Unstellung von Hochstspannungs-Erdungsalagen Aufden Betrieb Mit Starr Geerdetem Sternpunkt," *Electrotechnische Zeitschrift*, vol. 73, no. 10, pp. 333–337, May 1952.

[31] J. Nahman, and D. Salamon, "A practical method of the interpretation of earth resistivity data obtained from driven rod tests," *IEEE Trans. on Power Delivery*, vol. 3, pp. 1375-1379, Oct. 1988.

[32] H.R. Seedher, J.K. Arora and B. Thapar, "Finite expressions for computation of potential in two-layer soil," *IEEE Trans. in Power Delivery*, vol. 2, pp. 1098-1102, Oct 1987.

[33] F. Dawalibi, D. Mukhedkar, and D. Bensted, "Measured and computed current densities in buried ground conductors," *IEEE Trans. on Power Apparatus and Systems*, vol. PAS-100, pp. 4083-4092, Aug. 1981.

[34] F.P. Dawalibi, and N. Barbeit, "Measurements and computations of the performance of grounding systems buried in multilayer soils," *IEEE Trans. on Power Delivery*, vol. 6, pp. 1483-1490, Oct. 1992.

[35] P.J. Lagace, J.J. Houla, Y. Gervais, and D. Mukhedhar, "Computer aided design on a toroided ground electrodes in two-layer soil," *IEEE Trans. on Power Delivery*, vol. 2, pp. 744-749, Jul. 1987.

[38] J. Ma, F. P. Dawalibi, and R. D. Southey, "On the equivalence of uniform and two-layer soils to multilayer soils in the analysis of grounding systems," *Proceedings on the Institute Electrical Engineers—Generation, Transmission and Distribution*, vol. 143, pp. 49-55, Jan. 1996.

[39] J. Ma, F. P. Dawalibi, and W. K. Daily, "Analysis of grounding systems in soils with hemispherical layering," *IEEE Trans. on Power Delivery*, vol. 8, pp. 1773-1781, Oct. 1993.

[40] A. Sommerfeld, *Partial Differential Equations in Physics*. New York: Academic Press, 1949.

[41] Y.L. Chow, J.J. Yang, D.G. Fang, and G.E. Howard, "A closed form spatial Green's function for the thick microstrip substrate," *IEEE Trans. on Microwave Theory and Techniques*, vol. 39, pp. 588-592, Mar. 1991.

[42] R.M**.** Shubair, and Y.L. Chow, "Efficient computation of the periodic Green's function in layered dielectric media," *IEEE Trans. on Microwave Theory and Techniques*, vol. 41, pp. 498-502, Mar. 1993.

[43] *EPRI report, "Analysis Techniques of Power Substation Grounding System; vol. 1; Design Methology and Tests"* EPRI EL-2682, Oct. 1982.

[44] J.G. Sverak, "Optimized Grounding Grid Design Using Variable Spacing Techniques," *IEEE Trans. on Power Apparatus and Systems*, vol. PAS-95, pp. 362-374, Jan./Feb. 1976.

[45] Y. Gao, R. Zeng, X. Liang, J. He, W. Sun and Q. Su, "Safety Analysis of Grounding Grid for Substations with Different Structure", *IEEE International Conference on Power System Technology*, Vol. 3, pp. 1487-1492, Dec. 2000.

[46] M.C. Costa, M. L. P. Filho, Y. Mirechal, J. Coulomb, and J. R. Cardoso, "Optimization of Grounding Grids by Response Surfaces and Genetic Algorithms", *IEEE Trans. On Magn.*, vol. 39, pp 1301-1304, May. 2005.

[47] E. Bendito, A. Carmona, A.M.Encinas and M. J. Jimenez, "The External Charge Method in Grounding Grid Design," *IEEE Trans. On Power Delivery*, vol. 19,pp 118-123, Jan. 2006.

[48] F. Dawalibi and N. Barbeito, "Measurements and computations of the performance of grounding systems buried in multilayer soils," *IEEE Trans. on Power Delivery*, vol.6, pp. 1483-1490, Aug. 2002.

[49] J.A. Güemes, and F. E. Hernando, "Method for calculating the ground resistance of grounding grids using FEM," *IEEE Trans. on Power Delivery*, vol. 19, pp 595-600, Apr. 2004.

[50] C. Wang, T. Takasima, T. Sakuta, and Y. Tsubota, "Grounding resistance measurement using fall-of-potential method with potential probe located in opposite direction to the current probe," *IEEE Trans. on Power Delivery*, vol. 13, pp. 1128-1135, October 1998.

[51] W.Sun, J.He, Y. Gao, T. Zeng, W. Wu and Q. Su, "Study of Unequally Spaced Grounding Grids," *IEEE Trans. on Power Delivery*, vol. 10, pp. 716-722, Apr. 1995.

[52] *Canadian Electrical Safety Code Part I*, 20th ed, Safety Standard for Electrical Installations, 2009.

[53] S.Olafsson, and J.Kim, "Simulation optimization," *Proceedings of the 2002 Winter Simulation Conference*, pp. 79-84, Dec. 2002.

[54] D. Yan and H. Mukai, "Stochastic discrete optimization," *SIAM Journal on Control and Optimization*, vol. 30, pp. 594-612, Aug. 1992.

[55] W.K. Hastings,"Monte Carlo sampling methods using Markov chains and their applications," *Biometrika*, vol. 57, pp. 97 109, Apr. 1970.

[56] S. Geman and D. Geman,"Stochastic relaxation, Gibbs distributions and the Bayesian restoration of images," *IEEE Trans. on Pattern Analysis and Machine Intelligence*, vol.6, pp. 721-741, Jan.1984.

[57] A. Gelman, G. Roberts and W. Gilks, *Efficient Metropolis jumping rules, in Bayesian Statistics*. Oxford, United Kingdom: Oxford University Press, 1996.

[58] R.E. Kass, Carlin, B.P. Gelman and R.M. Neal, "Markov chain Monte Carlo in practice: a roundtable discussion," *The American Statistician*, vol. 52, pp. 93-100, Jul.1998.

[59] R.M. Neal, "Inference using Markov Chain Monte Carlo methods," Department of Computer Science, University of Toronto, Toronto, Report CRG-TR-93-1, 1993.

[60] R.M. Neal, "Suppressing random walks in Markov Chain Monte Carlo using ordered over-relaxation," Department of Statistics, University of Toronto, Toronto, Technical Report 9508, 1995.

[61] C.H. Papadimitriou, “On Selecting a Satisfying Truth Assignment,” *Proceedings of the Conference on the Foundations of Computer Science*, San Juan Puerto Rico, 1991, pp. 163-169.

[62] U. Schoening, “A Probabilistic Algorithm for k-SAT and Constraint Satisfaction Problems,” *Proceedings of FOCS*, New York NY, 1999, pp 410-414.